A multi-stage approach of simulating turbulence-induced vibrations in a wire-wrapped tube bundle for fretting wear prediction

Henri Dolfen[a,*], Jeroen De Ridder[a], Landon Brockmeyer[b], Elia Merzari[c], Graham Kennedy[d], Katrien Van Tichelen[d], Joris Degroote[a,e]

[a] *Department of Electromechanical, Systems and Metal Engineering, Ghent University, Sint-Pietersnieuwstraat 41, 9000 Ghent, Belgium*
[b] *Argonne National Laboratory, Lemont, IL, United States of America*
[c] *The Pennsylvania State University, University Park, Pennsylvania, United States of America*
[d] *Belgian Nuclear Research Centre, Mol, Belgium*
[e] *Flanders Make, Belgium*

Abstract

MYRRHA (Multi-purpose hYbrid Research Reactor for High-tech Applications) is a prototype of a Generation IV reactor that will be constructed in Mol, Belgium. It is a liquid metal fast reactor, using lead-bismuth eutectic (LBE) as a coolant. Flow-induced vibrations resulting in fretting wear could be of concern due to the high density of LBE. Additionally, a wire is wrapped around each fuel rod to preserve their mutual distance in the hexagonal array, which affects the flow pattern.

In this research turbulence-induced vibrations are investigated. Large-eddy simulation is a sound technique to acquire turbulent loads, but it is computationally demanding to combine this in a two-way coupled fluid-structure interaction (FSI) simulation. However, because accurate prediction of the vibration of cylinders subject to liquid flow typically requires a two-way simulation due to the added-mass effect, a methodology consisting of multiple steps is proposed. First, the modal characteristics of the pin are determined in a fully coupled FSI simulation of a bare bundle. The material properties used in this model are

*Corresponding author
Email address: henri.dolfen@ugent.be (Henri Dolfen)

modified to take into account the effect of the wire, which was determined experimentally beforehand. The resulting characteristics are then used to construct a realistic structural model, employed in a one-way simulation with turbulent loads from a large-eddy simulation of a wire-wrapped bundle.

In this structural model contact with neighboring rods and the hexagonal duct is detected, providing realistic boundary conditions to the rod and allowing to extract contact forces. These forces are further post-processed together with the sliding displacement to calculate work rates, which is an important parameter for fretting wear prediction. Two pins of a 19-pin bundle were investigated, the central pin and a pin located in one of the corners. The simulation is repeated for multiple friction coefficients, and its impeding effect of friction on sliding motions was confirmed to moderate fretting.

Keywords: Fluid-structure interactions, Computational Fluid Dynamics, Flow-induced vibrations, Turbulence-induced vibrations, Tube bundles, Fretting wear

1. Introduction

Generation IV nuclear reactors hold the promise of increased safety and reduced nuclear waste. One prototype of such a reactor called MYRRHA (Multipurpose Hybrid Research Reactor for High-tech Applications) is currently being developed at the Belgian Nuclear Research Centre SCK-CEN [1]. It is a liquid metal fast reactor (LFMR) that can work in both sub-critical and critical mode. For the former, it uses a particle accelerator to drive the reaction, making it a demonstrator of the Acceleration Driven System (ADS) concept. The reactor will also facilitate materials research and create isotopes for medical use. Furthermore it can be used for the demonstration of transmutation of long-lived nuclear waste, contributing to solving one of the drawbacks of nuclear energy, the long-term waste management.

One aspect of thermal hydraulic safety is flow-induced vibration (FIV). The long and slender fuel assemblies tend to vibrate under the loads imposed by the

coolant axially flowing between the fuel rods. In the design process, three steps were identified by Païdoussis [2] to accommodate for the effect of flow-induced vibrations. The first is assuring that the critical velocity for fluid-elastic instabilities is not exceeded. A second aspect is to avoid parametric resonances with harmonic fluid loads. A third one is to investigate turbulence buffeting and the associated damage mechanisms: fatigue and fretting. This research is situated in the third aspect: turbulence-induced vibrations (TIV) and consequences regarding fretting. MYRRHA uses lead-bismuth eutectic (LBE) as a coolant, which is about 10 times as dense as water, raising some vibration concerns. To preserve the distance between adjacent rods, a wire-spacer is wrapped helically around each pin. This enhances mixing, which is beneficial for heat transfer [3, 4]. The pressure drop still allows sufficient natural convection, a feature that contributes to the passive safety. The wire induces a strong secondary flow, as was demonstrated by Jeong et al. [5] for a sodium-cooled reactor using computational fluid dynamics (CFD). This latter aspect also highlights the need for research towards FIV. In the paragraphs below different techniques are discussed with their benefits and drawbacks, to motivate the research strategy chosen for this work.

The strict safety regulations result in high costs during the development phase. Using numerical simulations during this phase can alleviate some of these costs, and at the same time contribute to the design performance and safety such that unexpected failures and outages coming with a high economical cost can be avoided. Moreover they can provide physical understanding of the system that is sometimes hard to achieve with experiments. With the rise of computational power over the last decades, CFD has become a common way to investigate flows, and more recently also coupled fluid-structure interaction (FSI) simulations became widespread.

Examples of CFD work investigating the flow in wire-wrapped fuel bundles are the papers of Ahmad and Kim [6], Raza and Kim [7], Hamman and Berry [8], Sreenivasulu [9], Rolfo et al. [10], Jeong et al. [5], Merzari et al. [11], Brockmeyer et al. [12], De Santis and Shams [13] and Martin et al. [14] using

Reynolds-averaged Navier–Stokes (RANS) or unsteady RANS (URANS). In the latter work modeling the wire with a momentum source is explored, as the wire renders the meshing process complex and cumbersome. When turbulence is of concern, large-eddy simulations (LES) or direct numerical simulations are more sound, as in (U)RANS the turbulence is modeled rather than resolved, meaning that only the effect on the main flow is captured well. Examples of LES in a wire-wrapped bundle includes the work of Fischer et al. [15], Merzari et al. [11, 16] and Brockmeyer et al. [12, 17, 18]. The downside of large-eddy simulations is the higher computational cost, especially at an elevated Reynolds number. Recently a method has been proposed using URANS instead of LES, while still producing a fluctuating pressure field [19]. This Pressure Fluctuation Model generates a fluctuating random velocity and pressure field that satisfies the mean turbulent quantities. An OpenFOAM® implementation has been developed and tested on both a bare and wire-wrapped fuel pin [20]. An extensive review of CFD and experimental work on wire-wrapped fuel geometries can be found in Ref. [21], which broadly covers the technical challenges of LMFR thermal hydraulics and the research efforts done to address those.

When the turbulent, fluctuating pressure field is obtained through LES, it can be used as the excitation in a one-way coupled FSI simulation to obtain the displacement response. This has been done in earlier work to assess FIV in PWR [22–24] and LMFR [18]. It is assumed that feedback from structural displacement on the flow is negligible, as the displacements in TIV are usually rather small. An important aspect is however that the modal characteristics of a submerged structure are modified by an added mass and added damping, an effect that is not captured in a one-way approach. Nevertheless, only few examples were found in literature on two-way FSI of vibrating tubes using LES since this entails a high computational cost. Liu et al. have performed FSI on a cylinder in annular flow [25, 26] and small clusters of cylinders [27], loosely coupling large-eddy simulations to a beam element computational solid mechanics (CSM) model, although with a rather coarse CFD mesh. These kind of explicit formulations lessen the computational demand, as each time-step only requires

one evaluation of both solvers, but they become unstable for large added masses [28]. Nazari et al. [29] performed two-way LES-FSI on a simplified representation of the experimental setup of Hooper and Rehme [30], but it is not clear whether a strong or loose coupling scheme was applied. Benhamadouche et al. [22] used LES in a one-way FSI approach, however augmenting the model by lumping the added-mass of a single cylinder in quiescent flow obtained from a potential flow solution into the structural model.

Two-way coupled FSI simulations have been successfully used to determine the modal characteristics of cylindrical structures. De Ridder et al. [31] determined the added mass and damping of a vibrating cylinder in annular flow by coupling an unsteady RANS CFD simulation to a finite elements model. A flexible cylinder placed in a bundle of rigid cylinders was investigated as well. The results compared well against experiments and linear theory and have the advantage of being independent of empirical coefficients that appear in the fluid forces used in linear theory. Other examples can be found in the work of De Santis et al. [32, 33], in which the natural frequencies and damping ratios of cylinders in axial flow were determined. For a cluster of cylinders, the dynamics become more complex due to the inter-cylinder coupling caused by the presence of the fluid [34, 35]. The result is that each flexural mode corresponds to a range of natural frequencies and damping ratios rather than a single value. Using a similar approach as in [31], the modal characteristics of a cluster of cylinders were determined using two-way coupled CFD-CSM simulations by De Ridder et al. [36], the results of which are built upon in this research.

In this work, a procedure is developed to calculate the TIV response of a wire-wrapped fuel pin in a bundle in an efficient way, using a dedicated numerical approach for each aspect and combining the results in the end. The turbulence excitation load obtained via a large-eddy simulation is applied on a structural model augmented with modal properties determined via strongly coupled URANS-FSI simulations. A similar approach has been followed by De Ridder et al. for a single bare cylinder in axial flow [31, 37] in the frequency domain. In the current work contact detection with neighboring fuel pins is used,

to accurately represent the boundary conditions. Because of this a time-domain approach is preferred [38].

One of the main negative consequences of FIV in tube bundles is that it can cause fatigue, and when contact with other tubes or components occurs also fretting wear or damage due to impacts can be induced. In this research contact is continuously present once the effect of the initialization has vanished and the surfaces that are in contact exhibit sliding oscillations, as will be shown later on. This rubbing type of contact provokes fretting wear. Fretting wear is often the root-cause of fuel failure, recent works indicate that more than 70 % of fuel failures in PWR reactors are related to fretting [24, 39, 40]. Fretting is a complex wear process, resulting from highly non-linear contact dynamics. Numerical efforts have taken place to predict this phenomenon, often finite element models with stochastic forces representing the turbulence excitation load. An early example of work simulating the contact problem is Rogers and Pick [41], investigating heat exchangers. Shell-and-tube heat exchangers often have a large amount of cross-flow and there is typically a clearance between tubes and tube-supports to facilitate mounting and accommodate for thermal expansion, making them susceptible to fretting damage. They have often been subject of research using a numerical approach [42–45]. Similarly also steam generators [38, 46–49], CANDU fuel bundles [50–52] and more recently a complete fuel string [53], and grid-to-rod-fretting (GTRF) in PWR [24, 54–56] have been investigated. To the authors' knowledge, this kind of numerical analysis has not yet been performed for a wire-wrapped bundle geometry.

In the literature [57], a need to research fretting for MYRRHA has been identified, but fatigue on the other hand is not expected [57, 58]. Wear marks due to contact have been observed in real reactors with wire-wrapped fuel assemblies in hexagonal array [59]. The contact forces obtained from the simulations of present work can be used to calculate an estimate of the expected wear rate due to FIV, in order to meet this demand for fretting analysis.

This paper is organized as follows. Section 2 presents the overall methodology of this work in which 4 parts are distinguished. In section 3, section 4,

section 5 and section 6 each of these steps is discussed along with some intermediate results. The final results are discussed in section 7. Finally, the conclusions can be found in section 8.

Nomenclature

$a_{i,j}$	Amplitude of mode j on cylinder i (mm)
A	Area (m^2)
C_{ab}, C_{x1x2}, C_{y1y2}, C_{x2y2}	Coherence
D_f	Fillet diameter (mm)
D_i	Pin inner diameter (mm)
D_o	Pin outer diameter (mm)
D_w	Wire diameter (mm)
EI	Bending stiffness $(N \cdot m^2)$
f, f_k, f_{target}	Frequency (Hz)
F_a, F_b, F_N	Force (N)
$\vec{F}_i$	Contact force at time increment i (N)
FS, FS_a, FS_{x1}, FS_{x2}, FS_{y1}, FS_{y2}	Synthetic force signal (N)
h	Penetration depth (m)
$\dot{h}$	Penetration rate (m/s)
H	Hardness (Pa)
k	Dimensionless wear coefficient
K	Empirical wear coefficient (Pa^{-1})
L, L_1, L_2, L_3	Length (mm)
m_1, m_2	Linear mass density (kg/m)
P	Pin pitch (mm)
P_{aa}, P_{bb}	Power spectral density (N^2)
P_{ab}	Cross power spectral density (N^2)
P_h	Helical pitch (mm)
PW_a, PW_{new}, PW_{x1}, PW_{x2}, PW_{y1}, PW_{y2}	White noise signal
$\vec{r}_i$	Contact point coordinate vector at increment i (m)

s	Sliding displacement (m)
TF, TF_{new}, TF_{old}	Tuning factor
$u_{cl,i}$	Centerline displacement of cylinder i (mm)
V	Volume removal (m^3)
$\dot{V}$	Volume removal rate (m^3/s)
$\dot{W}_N$	Normal work rate (W)
α	α parameter of Rayleigh damping model (s^{-1})
β	β parameter of Rayleigh damping model (s)
ζ_j	Modal damping of mode j
μ	Friction coefficient
μ_f	Viscosity $(Pa \cdot s)$
ρ_f	Fluid density (kg/m^3)
$\phi_{i,j}$	Phase difference (rad)
$\omega_{n,j}$	Natural frequency of mode j (rad/s)

2. Methodology

The proposed procedure consists of four major parts, as summarized in Figure 1. First, experiments were conducted on both a bare and a wire-wrapped MYRRHA fuel pin in air to determine the modal characteristics, as part of the work of De Pauw [60], at the Belgian Nuclear Research Centre, see section 3. By doing so the effect of the wire on the *in-vacuo* modal properties was known and this information was used in the second part: two-way FSI simulations on a cluster of 7 bare rods in axial LBE flow, coupling a URANS CFD model to a finite elements CSM model. The effect of the wire was lumped into the CSM part of the coupled simulation, by adjusting the material properties. This part, performed at Ghent University, yielded the modal characteristics of the fuel pins in relevant flow-conditions, capturing the effect of the LBE flow and the inter-cylinder coupling brought forth by it. This step has been described in the work of De Ridder [36], but the relevant parts are briefly summarized in section 4.

The URANS turbulence modeling of the second step can accurately determine the added mass and added damping effect, but it fails to resolve the turbulent fluctuations that excite the structure. To obtain these, large-eddy simulations were performed at Argonne National Laboratory on a rigid 19-pin wire-wrapped fuel assembly. This yielded a sample of the pressure fluctuations acting on the walls of the structures, and this data was post-processed to obtain a synthetic force history to be used in the final step. A more detailed description of the LES is given in section 5.

For the fourth and final part, a structural model of a wire-wrapped fuel pin was constructed using finite elements. The material properties are tuned to match the modal characteristics of the rods subject to LBE flow, determined in the second step. In a time domain simulation, the structure was exposed to forces extracted in the third part from the LES pressure data, essentially resulting in a one-way FSI simulation, yet taking into account the most important effects of strongly coupled FSI: added mass and added damping. The presence of the neighboring pins was modeled, providing realistic boundary conditions and allowing the detection of contact and the computation of contact forces. These contact forces were further processed to estimate the wear rate. This final step is discussed in section 6.

3. Experiments on single bare pin and single wire-wrapped pin in air

Figure 2 depicts a wire-wrapped MYRRHA fuel-pin mock-up used to measure modal properties. Similarly a bare pin has been constructed, thus lacking the wire spacer. The hollow cavity was filled with pellets representing fuel pellets in size and density. The tube is instrumented with optical fiber Bragg grating (FBG) based sensors for strain measurements, involving an optical fiber on the rod's surface running in a helical way along the length. During the fabrication of the fiber the local refractive index is periodically modulated over a limited length. As a result the FBG acts as a band-pass filter when light is fed to it, transmitting all wavelengths except for a narrow-band around the so-

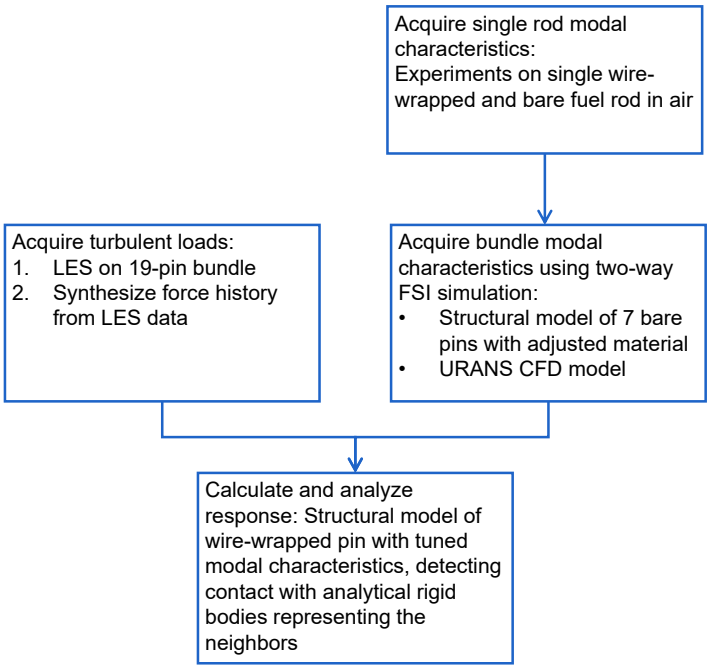

Figure 1: Flowchart of the general methodology.

called Bragg wavelength, which is reflected back. This wavelength is sensitive to certain perturbations, among which is mechanical strain. Keeping track of the Bragg wavelength allows measuring time-varying strains.

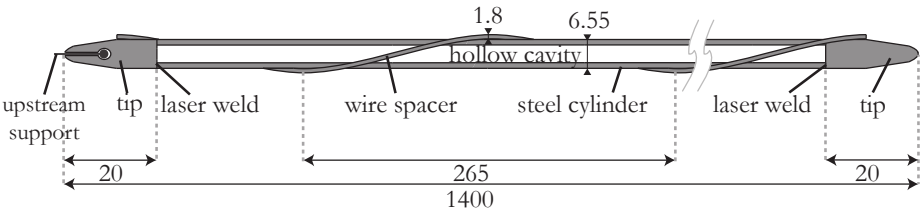

Figure 2: Drawing of the wire-wrapped pin used for the experiment determining the modal properties, the unit is mm. Adapted from [60].

Both the wire-wrapped and the bare fuel pin are excited using an air jet pulse, thus without physical contact. The pulse frequency can be governed up to 1 kHz. In [61] the measurement procedure has been validated on a

bare pin using a laser-Doppler vibrometer and an electrodynamic shaker. From these measurements of the vibration due to the pulse, the modal characteristics (frequency and damping ratio) of both a bare and a wire-wrapped fuel pin are known. A more in-depth description of the fuel pin mock-ups and measurement methodology can be found in the work of De Pauw [60].

4. Determining modal characteristics of bundle

This section describes the two-way FSI simulations that cover the second part of the general procedure, namely including the effect of the LBE on the modal characteristics. The technique has been elaborately described in the article of De Ridder et al. [36], but the parts most relevant to this work are summarized here for clarity.

4.1. Set-up

A bundle of 7 bare rods subject to axial LBE flow is simulated for different axial velocities. The geometric properties of the pin and bundle are shown in Table 2; the pin geometry and boundary conditions are also schematically displayed in Figure 3. They closely resemble the MYRRHA geometry. The properties of the fluid and structure are summarized in Table 3.

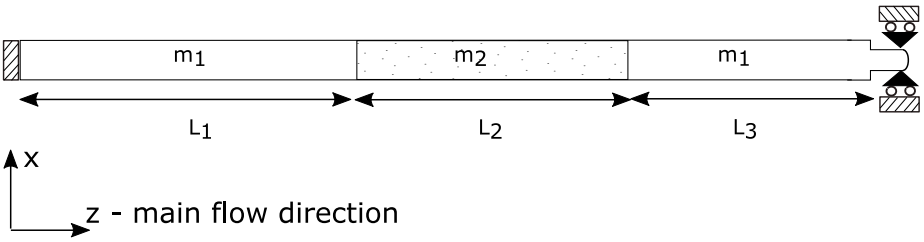

Figure 3: Sketch of fuel pin model, with structural boundary conditions and mass distribution. From [36].

For the FSI a partitioned approach [28] is chosen, calculating the flow and structure solution separately with dedicated solvers, only communicating the solution at the mutual interface. The advantage is that highly specialized solvers

Table 2: Geometrical properties of fuel pin for the coupled CFD-CSM model.

Parameter	Length (mm)
Pin outer diameter D_o	6.54
Pin inner diameter D_i	5.65
Pitch P	8.4
Length L	1400
L_1	627.5
L_2	600
L_3	172.5

Table 3: Fluid and structural properties (ρ_f: fluid density, μ_f: dynamic viscosity, E: elastic stiffness, I: area moment of inertia, m: mass per unit length).

Fluid properties		Structural properties		
ρ_f	μ_f	EI	m_1	m_2
10290 kg/m^3	0.0017 $Pa \cdot s$	10.3 $N \cdot m^2$	0.0664 kg/m	0.331 kg/m

can be used as black boxes, whereas the monolithic approach requires access to the governing equations in order to solve them simultaneously. The pressure and shear stresses acting on the interface are computed by the CFD solver and subsequently communicated to the structural solver, which on its turn computes displacements and communicates them back. In an implicit approach, this loop is iterated until convergence is achieved before advancing to the next time step. Since the density ratio between fluid and structure is close to 1, the physics will be strongly coupled and an implicit approach is deemed appropriate. In this work, the IQN-ILS (interface quasi-Newton with inverse Jacobian from a least-squares model) coupling algorithm is used to enhance convergence through a quasi-Newton minimization of the residual [62].

The mesh can be seen in Figure 4, it has 10 cells in wall-normal direction, 36 along the circumference and 200 cells in axial direction. URANS turbulence modeling is used, with the $k-\omega$ SST turbulence model to close the equations. A

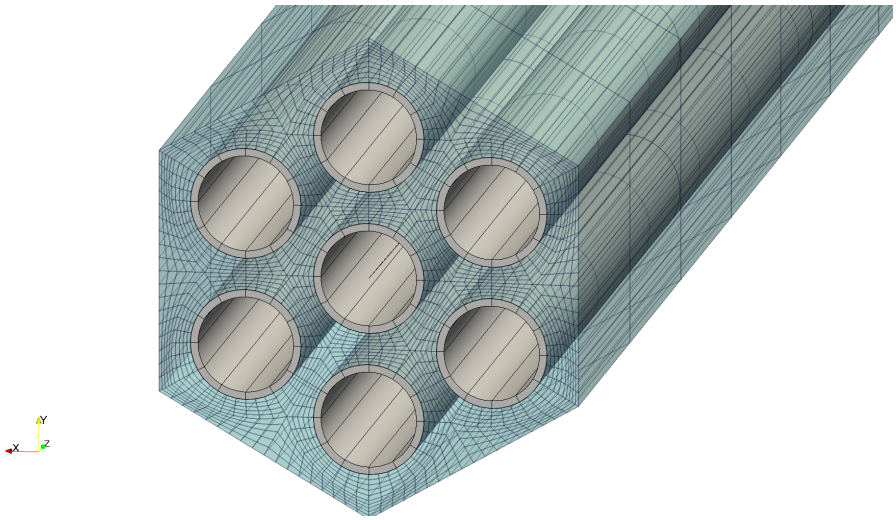

Figure 4: The CFD and CSM computational grids. From [36].

fixed velocity, turbulence intensity of 5% and length scale of 1 mm was imposed at the inlet and the outlet is kept at constant pressure. The rods and hexagonal duct are walls, thus having no-slip boundary conditions. A second-order discretization scheme is used, in both space and time, for all quantities. With a uniform inlet of 2 m/s this yields an average wall y^+ of 2.66, with more than 95 % of the cells having a y^+ below 5. This means the near-wall flow is resolved into the viscous sublayer and no wall functions are active.

The CSM part (also shown in Figure 4) comprises a finite element model using quadratic solid elements. The material properties are based on steel, but modified to represent a fuel pin, with the mass adjusted for the middle section to account for the presence of the fuel pellets, see Figure 3. Furthermore, the stiffness is tuned to lump the effect of the wire in the material properties of the bare cylinder, based on experiments, see previous section and [60]. This approach misses the effect of the cross-sectional shape of the wire-wrapped pin on the modal properties. Because the wire causes more turbulent mixing, the added damping is expected to be higher than this approximation captures. It is however argued that using lower damping is conservative with respect to FIV.

The wire also causes a global swirling motion [10], but its effect on the modal properties in a bundle has to the authors' knowledge not yet been investigated and is thus not included. The pins are fixed at the upstream end and simply supported (axial sliding allowed) at the downstream end, conditions that represent a support-active situation for all rods. The pin is in reality free at the downstream end in its neutral position, but likely to be supported by leaning against the adjacent rods as will also be shown later on.

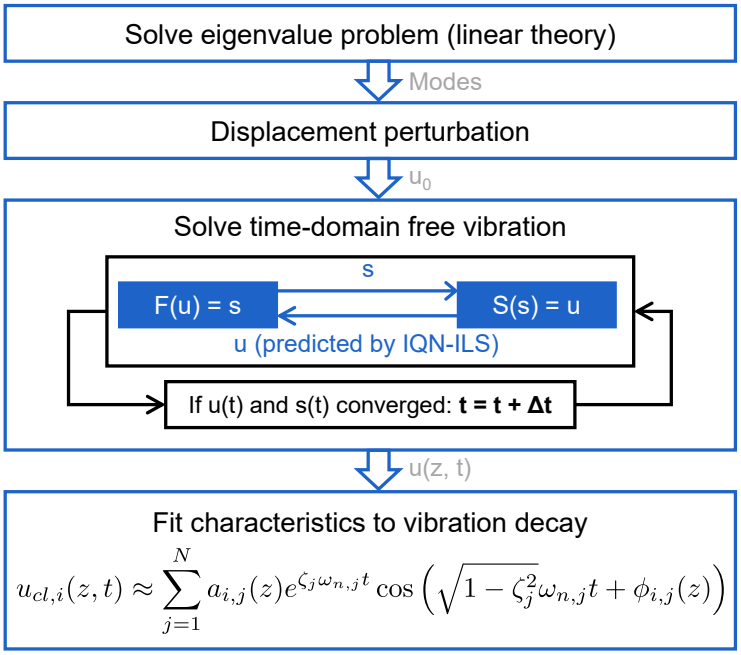

Figure 5: Flowchart of the sub-steps (based on [36]), in which F and S are the flow solver and structural solver respectively, u is the interface displacement and s the traction on the interface. The subscript cl denotes the centerline, $a_{i,j}(z)$ is the amplitude of mode j on cylinder i as a function of the axial coordinate z (mode shape), ζ_j is the modal damping ratio, $\omega_{n,j}$ the natural frequency and $\phi_{i,j}(z)$ is the phase difference. N represents the number of modes needed to achieve a good fit.

The complete procedure of determining the bundle modal characteristics of the 7-rod bundle is depicted in Figure 5. It comprises four steps, henceforth called "sub-steps" to avoid confusion with the four parts of the general procedure outlined in section 2.

In the first sub-step, the system is described using Euler–Bernoulli beam equations and potential flow. The motion of a single cylinder displaces fluid, which affects the neighboring cylinders and as such the displacement direction of all cylinders can be organized in patterns. For all patterns in a so-called "mode group", all cylinders have the same mode shape, but each pattern corresponds to a slightly different frequency and damping ratio. For a cluster of K cylinders, $2K$ different patterns exist. Due to this inter-cylinder coupling, the system is governed by an added-mass and damping matrix with non-zero off-diagonal values indicating the mutual interaction between cylinders. By solving the generalized eigenvalue problem corresponding to this formulation the modal frequencies and mode shapes are obtained.

Secondly, the mode shapes acquired in the first sub-step are used to perturb the displacement of the CSM model of the coupled CFD-CSM simulation, serving as an initial condition. The structure is kept in this position and the flow is allowed to settle in a steady CFD simulation, to obtain a suitable initial condition for the flow as well.

Subsequently, in the third sub-step, the structure is released and the free vibration is simulated in the time domain through a fully coupled FSI simulation and the displacement of the centerline is tracked and stored.

Finally, the centerline displacement is fitted to an expression of decaying vibration:

$$u_{cl,i} \approx \sum_{j=1}^{N} a_{i,j}(z) e^{-\zeta_j \omega_{n,j} t} \cos\left(\sqrt{1-\zeta_j^2}\omega_{n,j} t + \phi_{i,j}(z)\right), \tag{1}$$

with *cl* denoting the centerline, $a_{i,j}$ the amplitude of mode j on cylinder i at height z (expressing the mode shape), ζ_j the modal damping ratio, $\omega_{n,j}$ the natural frequency and $\phi_{i,j}(z)$ the phase. N represents the number of modes needed to achieve a good fit; in this case one mode was sufficient.

4.2. Modal characteristics

The resulting frequencies and damping ratios can be seen in Figure 6 for different flow rates. Due to the inter-cylinder coupling discussed above, mul-

tiple frequencies and damping ratios are obtained for each flow rate. For a 7-rod bundle each mode group theoretically contains 14 patterns, but only 9 frequencies and damping ratios are reported as due to the symmetry of the rods' arrangement 5 duplicate eigenvalues are present [34].

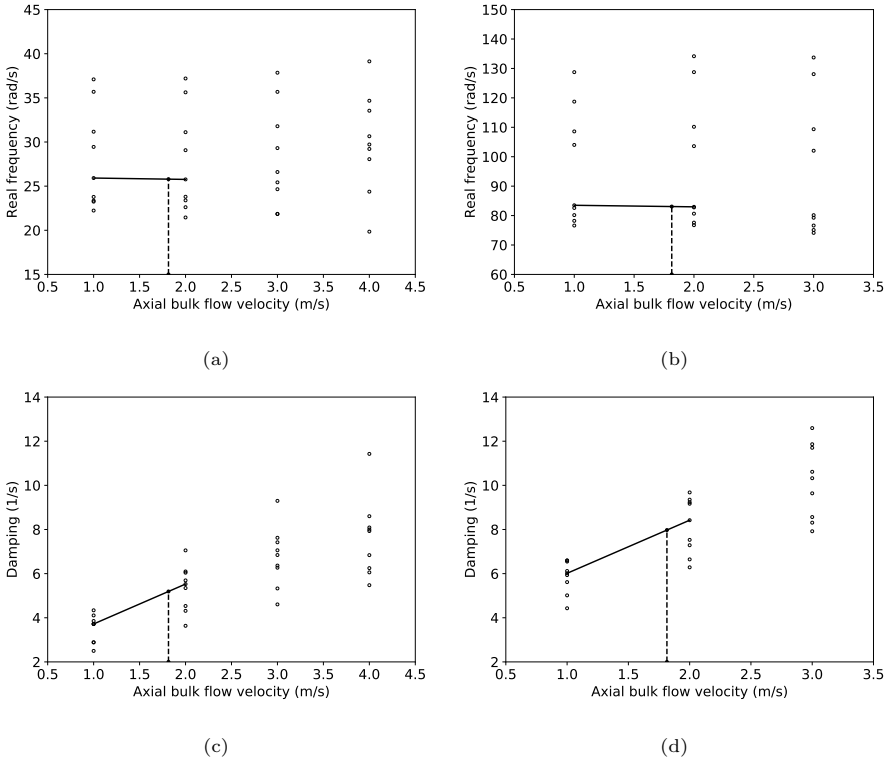

Figure 6: Modal characteristics at different flow rates: (a) frequencies mode 1 and (b) mode 2 and (c) damping mode 1 and (d) mode 2 (data from [36]). The lines indicate the interpolation to the velocity imposed in this work (1.81 m/s).

In Figure 6a and Figure 6b it is observed that the frequency range follows a rather horizontal trend with increasing flow rate, although the range seems to widen a bit both towards lower and higher frequencies. The modal damping ratio (Figure 6c and Figure 6d) clearly exhibits a rising trend with regard to the flow velocity due to the effect of the viscous forces. Both results agree well with linear theory [36].

For the current work, one frequency and one damping ratio of the first two modes are interpolated from the results at an axial velocity chosen close to the conditions in MYRRHA, in order to realistically represent the added damping experienced during operation. This velocity has a value of 1.81 m/s and will be kept constant in the third sub-step. The interpolation is each time performed using the median frequency or damping at 1 m/s and 2 m/s, see Figure 6. The obtained frequencies and damping ratios can be found in Table 4 and will be used in section 6.

Table 4: Modal characteristics interpolated at 1.81 m/s for the first two mode groups.

Mode group	Frequency	Damping
1	25.67 rad/s	5.15 1/s
2	82.44 rad/s	7.91 1/s

5. Determining turbulence load on bundle

In order to characterize realistically the turbulent loading acting on the structure, large-eddy simulations were performed at Argonne National Laboratory. For this the non-dimensional spectral elements code Nek5000 is used [63]. These simulations are described in the current section and correspond to the 3^{rd} part of the methodology.

5.1. Set-up

The simulated bundle consists of 19 wire-wrapped pins in a hexagonal duct as depicted in Figure 7 and the geometry of the CFD domain can be found in Table 5, corresponding to the MYRRHA fuel assembly design.

The flow is simulated at a bulk velocity of 1.81 m/s, being the one for which the data in the second sub-step was interpolated. The Reynolds number is 3×10^4, based on the hydraulic diameter. This corresponds to LBE at 200 $°C$, having a density of 10470 kg/m^3 and dynamic viscosity of 0.0024 $Pa{\cdot}s$ according to the relation between these fluid properties and the temperature of LBE [64].

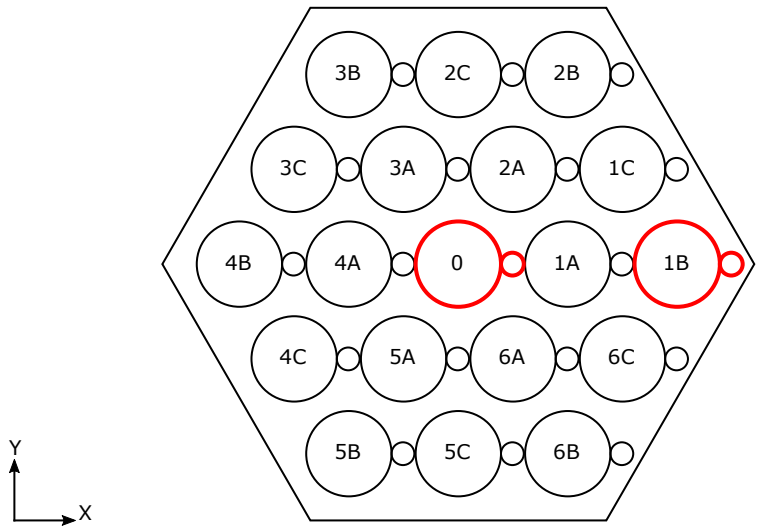

Figure 7: The 19-pin wire-wrapped bundle in a hexagonal duct. The rods of which the turbulence-induced vibrations are simulated are highlighted.

The periodicity of the geometry is exploited to reduce the computational cost, by using a periodic boundary condition at the upstream and downstream extremities of the domain and keeping the mass flow rate constant. As such only a single helical pitch needs to be simulated and the flow inherently behaves fully developed. The surface of the pins and duct are modeled as no-slip wall. A fillet was applied at the line contact between wire and pin, to facilitate meshing. The mesh consists of 1036800 elements, each further refined using an 11^{th} order polynomial. It is displayed in Figure 8, but note that for visualization purposes the element order in Figure 8b is limited to 5. A time step size of 5.4×10^{-6} s is used, and the pressure and shear forces acting on the fuel pins is recorded every 20 time steps, averaged over the face of the element. After the flow had settled, about 0.08 s of force history was recorded.

5.2. Forces

The forces originating from the flow and acting on the pins consist of a normal component, due to pressure, and a tangential component, due to wall shear stress. The resultant force is calculated along the circumference of each

Table 5: Geometric parameters of the LES mesh.

Parameter	Length
Pin diameter D_o	6.55 mm
Wire diameter D_w	1.75 mm
Fillet diameter D_f	0.7 mm
Pitch P	8.4 mm
Helical pitch P_h	262 mm

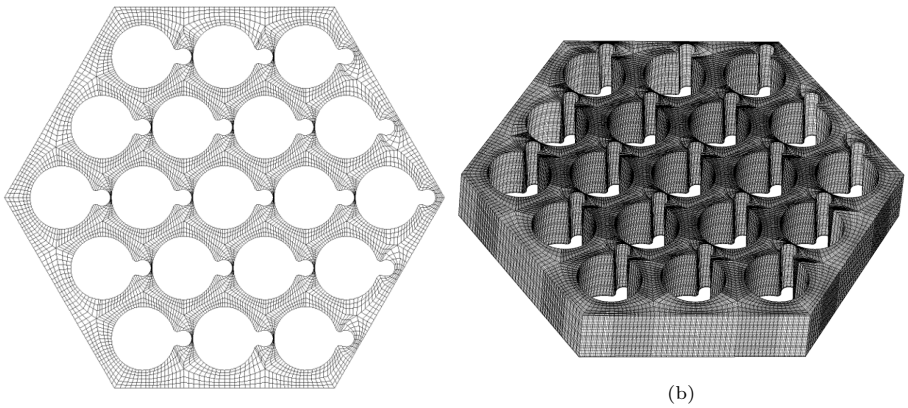

(a) (b)

Figure 8: Visualization of the mesh used for the LES: (a) front view showing the element only and (b) example of mesh with 5^{th} order elements. In reality an 11^{th} order polynomial is used, but for a clear visualization only a lower order version is displayed.

rod, such that a vector is obtained, varying along the height of the pin. The geometry can be seen as a repetition of $1/6^{\text{th}}$ of a helical pitch, stacked on top of each other and rotated 60° each time. Because of the periodic boundary conditions each $1/6^{\text{th}}$ of a pitch experiences the same forces, but in a rotated reference frame. This is exploited for plotting, by averaging the force data over the 6 slabs after applying the appropriate rotation. Also for calculating the Power Spectral Density (PSD) advantage is taken of this, by averaging the PSDs corresponding to each $1/6^{\text{th}}$ pitch, thereby improving the statistical convergence [18].

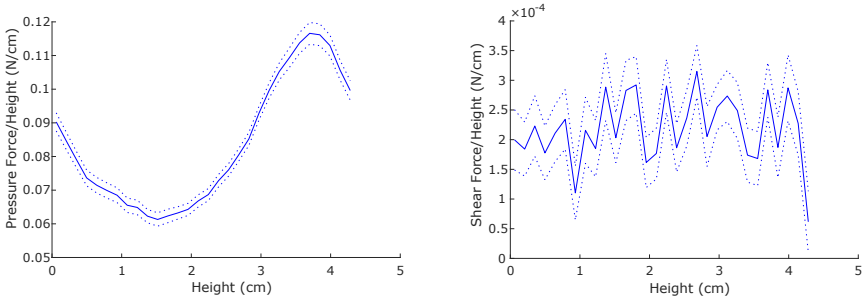

(a) (b)

Figure 9: Net force on the central pin caused by (a) pressure and (b) wall shear forces as a function of the height. The data is averaged for each $1/6^{\text{th}}$ of a pitch after applying appropriate rotation. The solid line represents the time average, the dotted line the standard deviation.

The resulting forces on the central pin as a function of height are shown in Figure 9. It can be seen that the force due to the wall shear stress is at least two orders of magnitude smaller than the pressure component and therefore it will be neglected in the remainder of the research.

Preliminary results revealed that the time history is too short for the structural calculation, even though the flow is fully developed and this duration is sufficient to characterize the flow. At the end of the LES simulation (0.08 s) contact has only just been established and the structural response is still in a transient phase. As the behavior under contact is of interest, more simulation time is needed. Instead of applying the loads directly, they were post-processed further in a synthetic force history which can be made arbitrary long. When using the longer, synthetic history it is indeed confirmed that the structure settles somewhere around 0.08 s, as will be seen from the results in the next section.

When turbulence-induced vibrations are investigated in literature, the excitation load is often modeled as band-limited Gaussian white noise, obtained by applying the inverse Fourier transform to a (semi-)empirical spectrum [44, 45, 51, 55, 56, 65] or one resulting from simulations [18, 24]. If forces are generated at multiple locations they are often assumed to be either uncorrelated [24, 66] or completely correlated [51, 65]. The latter is defended as being a conservative

estimate [51], while the former is used when the correlation length is assumed to be short. For the procedure in this work proper coherence is taken into account. This technique of synthesizing force data from LES results was demonstrated in the work of Brockmeyer [18], but for the sake of completeness it is explained below. It is worth mentioning that the generated force histories in this work are limited to a bandwidth of 10-4000 Hz.

The coherence of two force signals F_a and F_b is defined as

$$C_{ab}(f_k) = \frac{|P_{ab}(f_k)|^2}{P_{aa}(f_k)P_{bb}(f_k)}, \tag{2}$$

with P_{aa} symbolizing the power spectral density and P_{ab} the cross power spectral density. Both are estimated using the Discrete Fourier Transform (DFT). For each frequency, the coherence is a real number between 0 and 1, representing the similarity between signals.

$$P_{aa}(f_k) = \frac{1}{N}\left|\sum_{n=0}^{N} F_a(t)\exp(-j2\pi f_k n)\right|^2 \tag{3}$$

$$P_{ab}(f_k) = \frac{1}{N}\left|\sum_{n=0}^{N} F_a(t)\exp(-j2\pi f_k n)\sum_{n=0}^{N} F_b(t)\exp(-j2\pi f_k n)\right| \tag{4}$$

In these definitions N represents the number of discrete points in time and f_k the frequency.

A synthesized force history is constructed starting from the power spectral density of the force signal, which is computed as the square of the Fourier transform (see Eq. 3). By inverting this PSD, an artificial time history of arbitrary length can be generated. The number of possible signals resulting in a certain PSD is infinite, implying that a single PSD can be converted to an infinite number of unique time histories. A random white noise function can be applied to the phase, and by using the same white noise proportional to the coherence (see Eq. 2) of two signals, the coherence of the output signals can be matched to that of the input signals. It is not practically feasible to do this for each grid point on the surface of the structure, so the vector sum of forces on each $1/6^{\text{th}}$ pitch is used as input of the scheme [18].

The synthetic force-time history (FS) is generated by replacing the phase of the original signal with the one of a white noise signal. This is done in the frequency domain, after which the inverse Discrete Fourier Transform is used to generate a time series. The white noise is represented by $PW(f_k)$, which is strictly speaking not a PSD, but a squared series of complex Fourier coefficients, each having a magnitude of 1 as the amplitudes should not be modified.

$$FS_a(t) = \sum_{f_k=0}^{F} \left(PW_a(f_k) \cdot P_{aa}(f_k)\right)^{1/2} e^{j2\pi f_k t} \tag{5}$$

For each location at which a force-time history needs to be generated, a different white noise signal is generated (PW_{new}). However, in order to preserve the coherence between different force signals, this white noise signal is modified by reusing a portion of the white noise of the signal with which coherence is desired. The force histories are sequentially created for each $1/6^{\text{th}}$ pitch, starting at the bottom of the rod and continuing until the entire length of the rod (which is longer than just the CFD domain) is covered. After generating the first synthetic force histories FS_{x1} and FS_{y1} for the first $1/6^{\text{th}}$ pitch (that are also constructed to have the correct coherence), the white noise of the second $1/6^{\text{th}}$ pitch is generated as follows.

$$PW_{x2}(f_k) = PW_{x1} \cdot C_{x1x2} + PW_{new} \cdot (1 - C_{x1x2}) \tag{6}$$

$$PW_{y2}(f_k) = PW_{x2} \cdot C_{x2y2} + PW_{y1} \cdot (C_{y1y2} - C_{x2y2}) + PW_{new} \cdot (1 - C_{y1y2}) \tag{7}$$

Note that the magnitude of the white noise Fourier coefficient (equal to 1) is preserved. As such FS_{x1} has proper coherence with FS_{x2} and FS_{y2} with FS_{y1} as well as FS_{x2}. Continuing the procedure like this results in a set of force-time histories in which each signal has proper coherence with the perpendicular component as well as the upstream and downstream signals.

Force-time histories were generated for all slabs of all pins. Two pins were chosen to investigate further based on an analysis of the force signals. In Figure 10 the resultant force on each pin is shown as an average over time. The

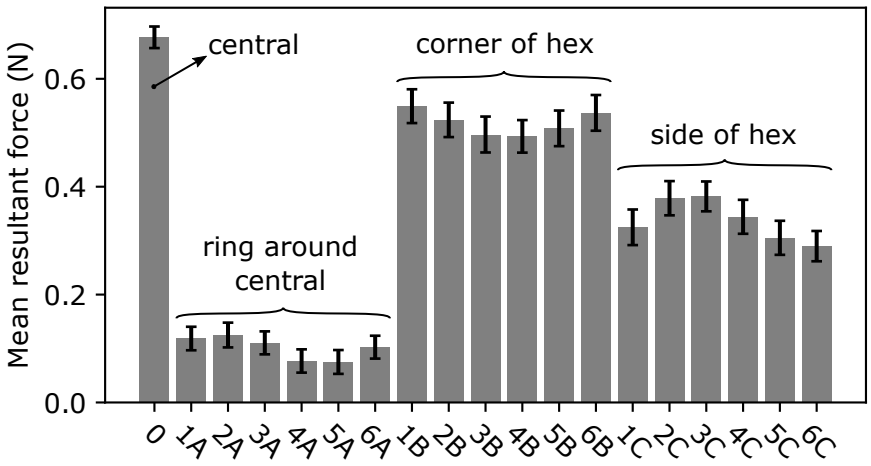

Figure 10: Resultant force on the pins, averaged over time. The standard deviation (over time) is also indicated. The name of the pins on the horizontal axis correspond with these in Figure 7.

standard deviation is also shown, indicating the fluctuating nature of the forces. In this figure distinct groups can be discerned, and they correspond to the groups that were already used to index the bundle in Figure 7. The time-averaged vector sum is seen to be largest for the central rod. Moving outwards, it is smallest for the inner ring of rods and larger for the outer ring, the corner rods (group "B") experiencing the largest forces. The fluctuations seem to grow when moving outwards. It is chosen to investigate the pin 0 (the central pin) and pin $1B$ (a corner pin), as they experience the highest force, pushing them against the neighboring structures. As will be seen in the next section, the contact force plays an important role in the work rates and wear. Additionally, pins of the outer ring also experience large fluctuations, which may result in more rubbing and thus higher wear rates.

6. Structural simulation of single flexible pin including contact detection with rigid neighbors

In this section the last step of the procedure outlined in section 2 is explained. The modal characteristics obtained in section 4 and turbulence excitation load from section 5 are combined into a structural model.

The structural simulations are performed using the finite element method in the software package Dassault Systèmes® Abaqus® 6.14. A CSM model of a wire-wrapped fuel pin was constructed, with the same geometric parameters as used for the LES simulations (Table 5), but with a length of 1.4 m and an inner diameter of 5.65 mm as was the case for the two-way FSI simulations of section 4. This corresponds closely to the MYRRHA fuel pin geometry as stated earlier. The wire, while wrapping around the rod, rotates from the x-axis to y-axis (counter-clockwise) with increasing z-coordinate, as can also be seen from Figure 11. At the most upstream position ($z = 0$) the wire is aligned with the x-axis. The mesh is extruded from a cross-section containing 261 elements and then twisted according to the helical pitch. With 513 axial divisions this results in a mesh of 133893 quadratic, hexahedral elements. The mesh is depicted in Figure 11.

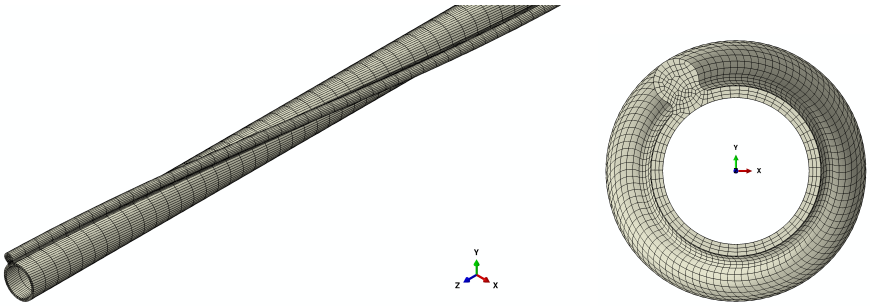

(a) (b)

Figure 11: CSM mesh: (a) isometric view and (b) top view.

Two materials were used: one material represents the heavier parts (mimicking presence of fuel) and has a density of 38871.8 kg/m^3 (this is higher than the

density of UO_2, because all of its mass is lumped into the hollow rod), the other material is modeled after steel with a density of 7850.0 kg/m^3. This results in a mass distribution equal to the one used for the two-way FSI as can be seen in Figure 3. Both materials have a Young's modulus of 183 GPa and a Poisson's ratio of 0.3, which resembles steel at the given temperature of 200 $°C$.

From the previous step (section 5) force-time histories are obtained for each $1/6^{\text{th}}$ of every helical pitch and are applied as a body force on the corresponding slab, acting as the excitation load. Given the length of the pin, a total of 66 force signals are used, 33 in x-direction and 33 in y-direction. As the pin does not contain an integer number of wire pitches, the most downstream force does not act on a complete $1/6^{\text{th}}$ pitch and is scaled accordingly.

This mechanism of transferring fluid loads to the structure result in a kind-of one-way coupled FSI simulation, hence no feedback is given from structure to fluid. Added mass and added damping effects are captured by tuning the material properties to match the modal characteristics obtained from the full FSI simulation of the second step.

The first mode frequency is matched to the median frequency of the first mode group, interpolated at a flow velocity of 1.81 m/s: 25.67 rad/s (see Figure 6a and Table 4). This is done by multiplying the densities of both materials with a tuning factor TF. The Lanczos algorithm [67] is used to determine the natural frequencies of the structural model. In these simulations the pin is clamped at the upstream end and pinned at the downstream end, as was the case for the two-way FSI simulations section 4. As such the boundary conditions have no influence on the difference in modal characteristic, and the effect of added mass and damping is isolated better. The tuning factor is obtained by iterating the following equation:

$$TF_{new} = TF_{old} \cdot (f/f_{target})^2, \tag{8}$$

in which the frequency f is updated using the Lanczos algorithm until it matches the target frequency. After a few iterations TF converged to a value of 2.49.

The added damping effect was modeled using structural Rayleigh damping,

which was added to both materials. The Rayleigh damping parameters α and β were determined by solving the following set of equations:

$$2\zeta_j\omega_{n,j} = \alpha + \beta\omega_{n,j}^2, \tag{9}$$

canwith $\omega_{n,j}$ and ζ_j the eigenfrequency and damping ratio of mode j. This set of equations is solved using the natural frequency and damping for the first two modes, interpolated at 1.81 m/s from the results in the second step as can be found in Table 4. For α a value of 9.71 s^{-1} was calculated and for β 8.99×10^{-4} s.

After the tuning procedure it was checked that the target first mode frequency and damping was obtained, by applying a small force in the middle and subsequently releasing the deformed rod into a free vibration. This method of tuning material properties to model the added mass and added damping effect has been tested by De Santis and Shams [68] and it was found that the results compared well to two-way coupled FSI simulations.

When the material properties are tuned and verified, the upstream boundary condition is changed such that rotations are allowed around the x-axis, while the other 5 degrees of freedom are constrained. This closely resembles the effect of the rails on which the pins will be mounted using a key-slot mechanism. The clamping at the downstream position is removed allowing it to move freely, nevertheless the displacement will be limited by contact with the neighboring rods. Contact detection is implemented, and when it occurs it is strictly enforced such that no penetration is possible. Only the rod under investigation will be subjected to the force history, the neighboring rods are modeled as analytical rigid bodies.

In reality some contact damping can be present as well, due to a squeeze-film effect [43, 69]. When the rods directly move towards each other just before contact, the liquid in between has to be evacuated, during which some energy is dissipated. This effect is not captured in this one-way simulation approach. However, as will be seen from the results, the contact is continuously present after the structure has settled such that only limited normal relative motions

take place. This makes it acceptable to omit this effect.

The geometry of the rod bundle makes the locations where contact can occur predictable, as it will always be the wire contacting a patch of the neighboring rod facing that wire, or a patch on the rod facing the wire of the neighboring rod. A wire will never contact the wire of a neighboring rod, because at each height the wire of neighboring rod closest to the wire is at the opposite side, as can been seen in Figure 7. Using this predictability, the contacts are detected in pairs that are stipulated by the location. The surface of the mesh is subdivided in patches, and each patch is assigned exactly one analytical rigid body as "contact partner." This saves computation time, as only the points that can possibly have contact are checked, and for each of this points only its "contact partner" is checked rather than all analytical rigid bodies. These bodies are cylinder parts, as can be seen from Figure 12. They are drawn partially, but actually extend to infinite length. The wire is approximated as a straight cylinder at an angle, tangent to where the real wire would be at the most probable location for contact, which can most clearly be seen from Figure 12e.

In the work of Brockmeyer [18], contact was assumed by rigidly connecting neighboring rods and orders of magnitude difference in vibration amplitude was found in case of a free rod bundle as compared to a bundle in which fixed contacts were assumed. Contact assumptions are therefore a strong source of uncertainty according to Merzari et al. [63]. The difference with this work is that here contact is not assumed, but the occurrence of it is detected. The central rod is free to move under influence of the fluid loads, much like a cantilevered beam, until it encounters one of the neighbors, engages in a contact interaction and is subject to a reaction force that restrains its motion. Comparing Figure 12a to Figure 12b and Figure 12c to Figure 12d, one can see that due to the dense packing of the bundle, free motion of the rods is rather limited. It must be noted nevertheless, that this work is not free of uncertainties introduced by assumptions since the neighboring rods and wires remain rigid. The results should thus be interpreted with care. Simulations with fully flexible bundles are at this stage of the research out of scope, as it increases the complexity and

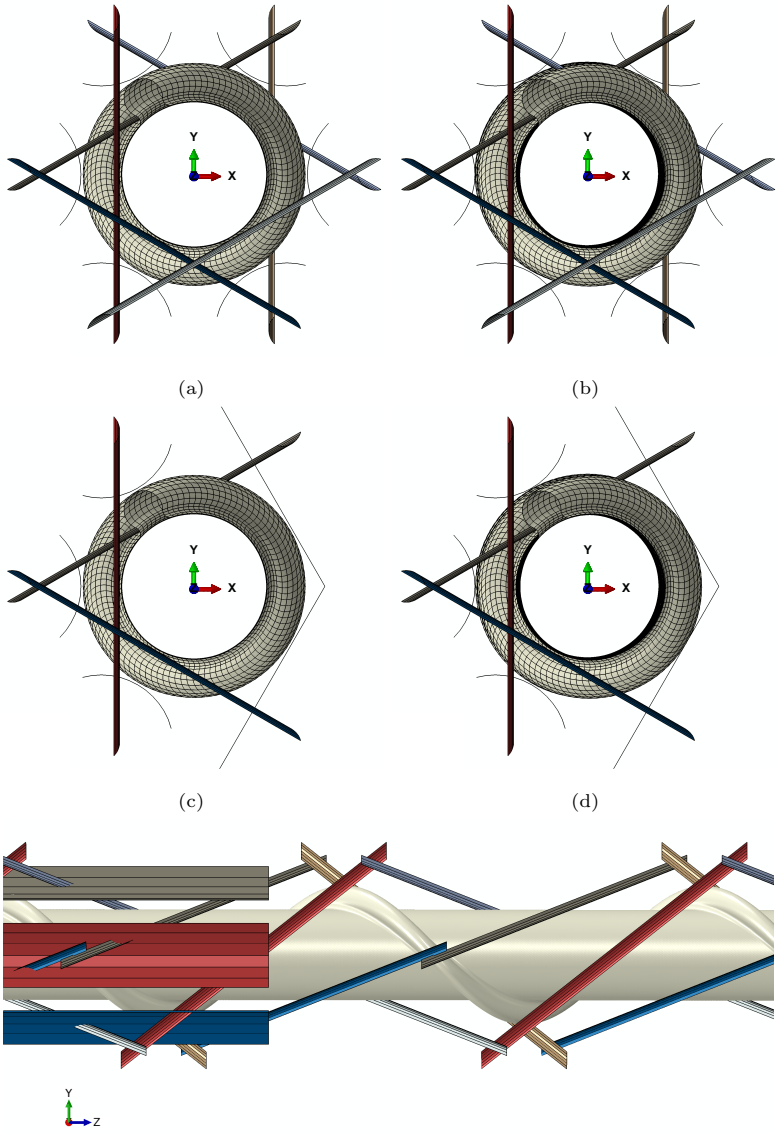

Figure 12: The CSM mesh together with the analytical rigid contact bodies, which extend to infinity but are only partially drawn. (a) The undeformed central pin, (b) the pin in deformed state after 5 s simulation time, (c) the undeformed corner pin, (d) the deformed corner pin (also at 5 s) and (e) a side view of the central pin. For (a-d) only the exterior surface is shown. The model shown in (e) has been scaled along the z-direction in order to show the contact bodies clearly.

computational requirements.

The wear model of Archard is a popular choice in literature to estimate the fretting wear, because of its simplicity.

$$dV = k(F_N/H)ds \tag{10}$$

Here dV is the infinitesimal volume removal, k a dimensionless wear coefficient, H the hardness of the softest material, F_N the normal force and ds the infinitesimal sliding displacement. Also a formulation based on the contact pressure exists, but because of the large element size compared to the contact area, the mesh resolution is deemed insufficient to accurately resolve the contact pressure and contact area. It is thus preferred to work with the force, being an integrated quantity, instead. This equation can be reworked to obtain the volume removal rate $\dot{V}$ $(m^3 s^{-1})$ related to the normal work rate $\dot{W}_N$ (W).

$$\dot{V} = K \cdot \dot{W}_N \tag{11}$$

In this formula H and k were combined into the empirical wear coefficient K (Pa^{-1}), which in general depends on the fretting regime, mainly dictated by sliding amplitude and normal force magnitude (for a set of materials in a certain environment) [70]. Whenever work rate is mentioned in the remainder of this paper, this refers to the time-averaged normal work rate, unless mentioned differently. The work rate is computed by integrating the normal force over the sliding distance for a certain time period Δt:

$$\dot{W}_N = \frac{1}{\Delta t} \int_{\Delta t} F_N ds. \tag{12}$$

In the case of a numerical simulation, this is discretized using the trapezoid rule:

$$\dot{W}_N \approx \sum_{i=0}^{N-1} \dot{W}(t_{i+1/2}), \tag{13}$$

$$\dot{W}(t_{i+1/2}) = \frac{1}{t_{i+1} - t_i} \cdot \left|\left| \left(\frac{\vec{F}_{i+1} + \vec{F}_i}{2} \right) \times (\vec{r}_{i+1} - \vec{r}_i) \right|\right|. \tag{14}$$

In this last equation $\vec{F}_i$ represents the contact force and $\vec{r}_i$ the coordinate vector at time increment i. By using the norm of the vector product, it is ensured that only the normal component is included. This does not hold at initiation or interruption of a contact because then r_i and r_{i+1} are not both on the surface, but these events are rare as will be shown later on, since the contact remains continuously present once the structure has settled. The terms of Eq. 13 will be referred to as the instantaneous work rates. The work rates can be computed for all mesh nodes engaging in contact. All nodes belonging to the same patch, i.e. interacting with the same neighbor and being directly adjacent to other nodes engaging in the same contact interaction are assumed to form one wear scar. Their work rates are simply summed to achieve the work rate of that wear scar and finally computing its volume removal rate following Eq. 11.

An important factor affecting the work rate and consequently the wear is the friction coefficient μ [71], especially when a preload is present [43]. Moreover it has been found that higher friction coefficients are associated with lower work rates [43, 45, 50, 56, 72], because friction impedes sliding. From experience with fretting experiments in the FRETHME facility at the Karlsruher Institut für Technologie (KIT) for the contact between steel specimens in presence of LBE at MYRRHA representative conditions [70, 73] the dynamic friction coefficient is estimated to lie between 0.08 and 0.2*. This is rather low and could indicate that the LBE offers lubrication to some extent. Determining the exact frictional behavior and modeling it afterwards is a research topic on itself and beyond the scope of the current work. To have an indication of the effect of friction on the results however, the simulations are repeated for different friction coefficients. A Coulomb friction model is used, but as the static friction coefficient is unknown and the dynamic friction coefficient is only roughly known, they are assumed to be equal. Also in related literature often a single friction coefficient is used [43–45, 50, 53, 72, 74–76]. A summary of the simulations can be found in Table 6. The friction coefficient μ ranges from 0.0 to 0.3 and for each situation 4 or 5

*Personal communication with the authors of [73].

Table 6: Overview of the simulations.

Pin	μ	Simulated time (s)
Central	0.0	5.0
	0.1	4.0
	0.2	4.0
	0.3	4.0
Corner	0.0	5.0
	0.1	4.0
	0.2	3.85
	0.3	4.0

seconds were simulated. Due to the non-linear nature of the simulation, namely discontinuities associated with contact and friction, convergence issues can arise. Especially the transition between sticking and slipping often causes numerical difficulties [44]. The nominal time increment of about 1.335×10^{-4} s is therefore allowed to decrease. For the corner pin simulation with $\mu = 0.2$ this was at a certain point not sufficient to overcome the discontinuities, and convergence was not achieved beyond 3.85 seconds. A simulation typically needed around 40 days on 36 2.6 GHz cores.

7. Results and discussion

This section discusses the results of the final stage of the procedure, which is also the main outcome of the research. In the discussion below several references will be made to specific contact locations. As was explained in the previous section, the contacts are detected in pairs. The locations will be denoted with either the word “ROD” or “WIRE” for the central rod, indicating which part of the pin participates in a contact interaction. The interaction always happens with the other component of the rigid neighbor, i.e. when a wire comes into contact with something it will always be with a rod part and vice versa. In the case of the corner pin, optionally the word “HEX” follows, which means that

the contact does not happen with a neighboring rod, but with the hexagonal channel. This word is followed by a digit, ranging from 1 to 6. This indicates the axial location in number of helical pitches, 1 indicates the most upstream pitch and 6 the most downstream pitch. The second digit further specifies the location and indicates the radial position. The number 1 means contact occurs with the neighbor in the positive x-direction (right neighbor in a top view) and the numbers increase counter-clockwise. Note that the increasing of this digit also corresponds to moving more downstream. One exception is the contacts with the hexagonal duct, where the second digit is either 1 or 2, 1 being a contact at the lower half (negative y-coordinate) of the channel and the 2 with the upper half. Also here a higher number means a more downstream position.

7.1. Contact forces

The simulation allows to extract the normal contact force for each point, as can be seen in Figure 13. The figure also shows the points where contact detection is enabled (force data is present) and where it is not (because occurrence of contact is judged unlikely). The corner pin with $\mu = 0.2$ is shown and the figures show that the contact happens with the hexagonal duct at the most downstream pitch. Besides the contact forces, also the displacements are known as well as the type of contact: sticking or slipping.

The normal forces at the contact locations are plotted as a function of time in Figure 14 for the central pin with $\mu = 0$ and Figure 15 for the corner pin with $\mu = 0.1$. Results for other pins are very similar. It is found that contact occurs persistently at two locations, independent of the friction coefficient. For the central pin these locations are WIRE-6-1 and ROD-6-3, for the corner pin WIRE-HEX-6-1, WIRE-HEX-6-2. To enhance the clarity also a reference to Figure 7 is made. For the central pin (pin 0), WIRE-6-1 means that at the most downstream wire pitch, the wire of pin 0 contacts the rod of fuel pin 1A. ROD-6-3 means that at the most downstream pitch, a part of the rod contacts the wire of pin 3A. For the corner pin (1B), WIRE-HEX-6-1 and WIRE-HEX-6-2 mean that in the most downstream helical pitch, the wire of pin 1B touches

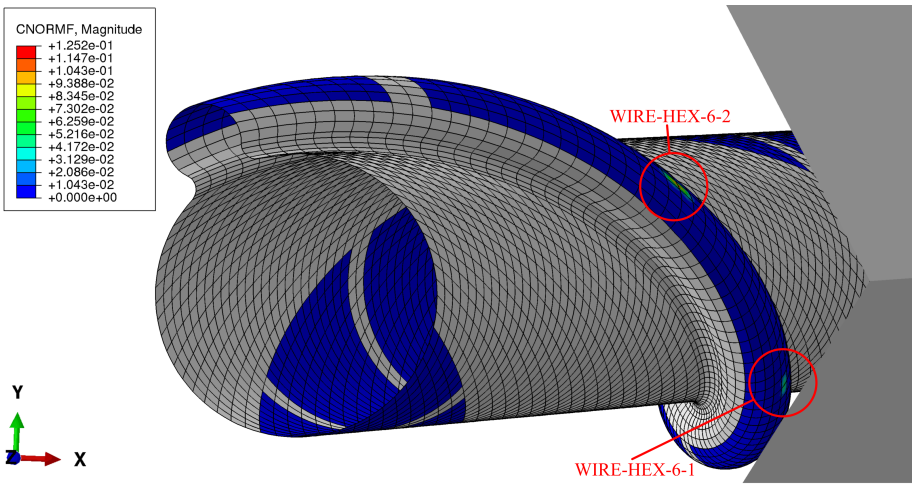

Figure 13: Normal contact force for the corner pin with $\mu = 0.2$, after 0.376 seconds. The hexagonal duct is partially drawn in order not to hide the pin, the neighboring rods and wires are not shown. Two contact locations can be seen, WIRE-HEX-6-1 and a larger force at WIRE-HEX-6-2. No contact is detected for the grey colored parts as the occurrence of contact is judged unlikely there.

the hexagonal duct twice, at each side of the rightmost corner. More central locations also contact occasionally, around the first initiation of contact shortly after the beginning of the simulations. These locations are not consistently the same when μ is changed. There the contact also only lasts for a brief period and is associated with a peak in the contact force, as can also be seen from Figure 14 and Figure 15. Impacts are indeed expected during transient situations, such as the starting of pumps or accidents. Outside of these events, negligible impacting should be present. Therefore no attention will be given to the first moments of the simulation. For the locations where contact is maintained, it can be seen that the normal force oscillates around a constant mean value. The amplitude of this oscillation varies both with μ and the pin under investigation.

The general behavior is that the pin leans against the supporting neighboring rod at a downstream position, this is to be expected for a pin that is essentially a kind of cantilevered beam. Due to the steady component around which the

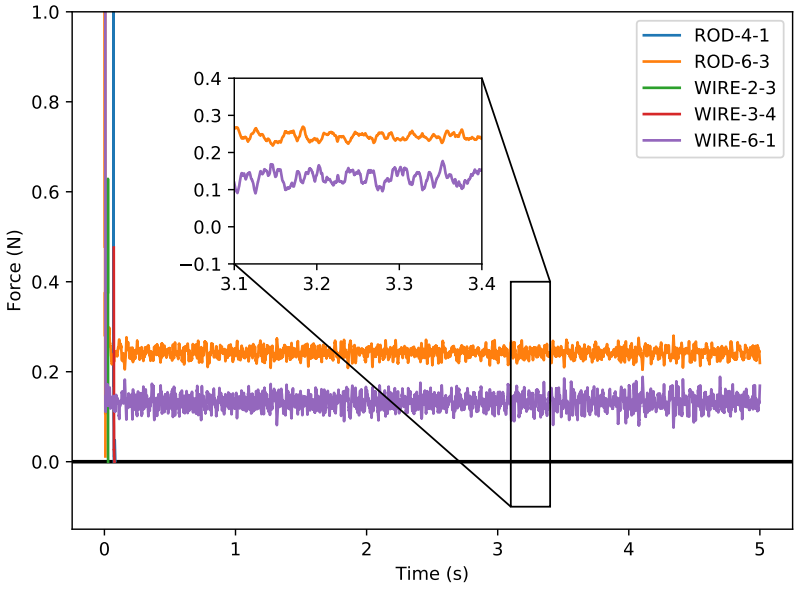

Figure 14: Normal forces on the central pin for the case where $\mu = 0$.

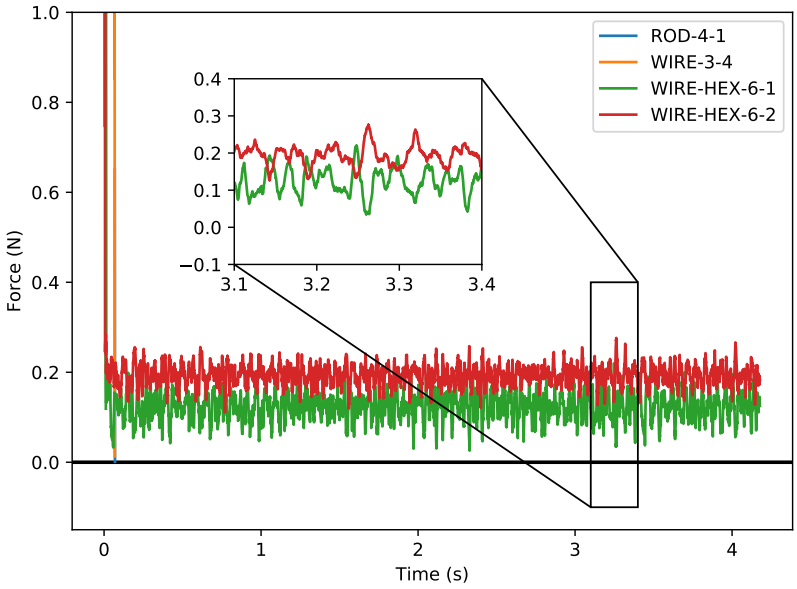

Figure 15: Normal forces on the corner pin for the case where $\mu = 0.1$.

forces oscillate, the rod is kept in place against two of its neighbors (central pin) or the hexagonal duct (corner pin). A rubbing motion is still possible however, as will be seen in the following sections.

When multiple rods would lean against each other the contact forces could accumulate for some rods, which is in this case not covered due to the rigid assumption of the neighbors. Simulating a fully flexible bundle is computationally expensive and beyond the scope of the current work. When this effect would occur larger displacements are present overall, which means the stiffness gains more importance in the force equilibrium, tempering the accumulation effect. It is expected that, although this effect could change the absolute quantities presented in this section, the conclusion of this paper would not be substantially affected.

7.2. Global deformation

The behavior of the pins can also be assessed by looking at the global displacement, as depicted in Figure 16. In this figure the bending of the central pin (with $\mu = 0$) can be observed, exaggerating the displacement was however required for a clear visualization. The undeformed state is drawn as well. The biggest displacement occurs at the downstream end, this is most clearly visible in the XZ-plane. As was discussed previously, the contact also occurs close to the downstream end.

These visualizations give an idea of a static deformation, around which a vibration occurs. It looks globally the same for all cases investigated, therefore only one figure is shown. The centerline has been tracked at a position halfway the rod ($z = 0.7\ m$), which is indicated by a dashed line in Figure 16. The observed motion in the XY-plane is displayed in Figure 17.

Due the global bending, this point moves away from its initial position and reaches a new quasi-equilibrium position, around which it vibrates in both x- and y-direction. This new equilibrium does not differ much for the various cases, so the figure is only drawn for the central pin with $\mu = 0$. The amplitude in both directions can be seen to be in the order of $1 \times 10^{-5}\ m$. An abrupt direction

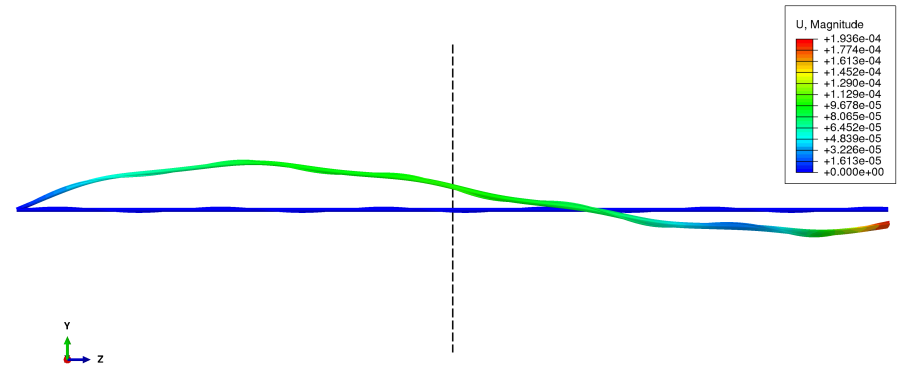

(a)

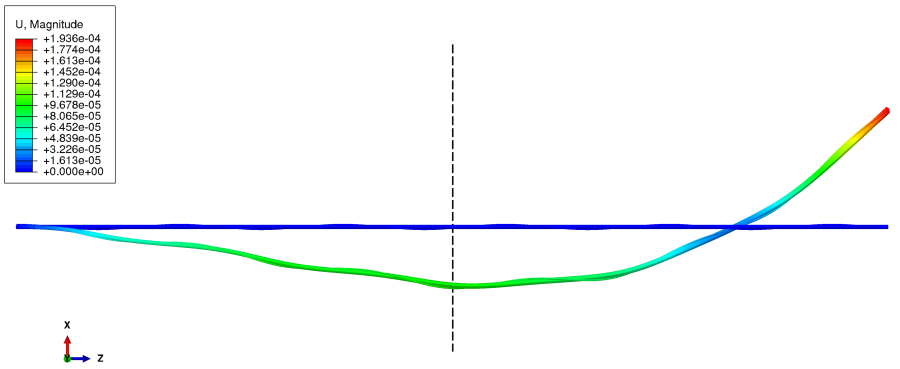

(b)

Figure 16: Global deformation in (a) YZ-plane and (b) XZ-pane of the central pin with $\mu = 0$ after 20000 time steps. The displacements have been scaled by a factor 1000 for visualization purposes. The rod is colored by the (unscaled) displacement magnitude. The dashed line indicates the midplane of the rod, $z = 0.7\ m$.

change can be seen at the leftmost part of the plot. It is hypothesized that this is related to the initiation of contact at WIRE-3-4, a nearby position. This is a rather impacting contact, so it is observed to end soon afterwards and is also associated with a spike of the contact force of about 0.5 N, as can be seen from Figure 14 around $t = 0.07\ s$.

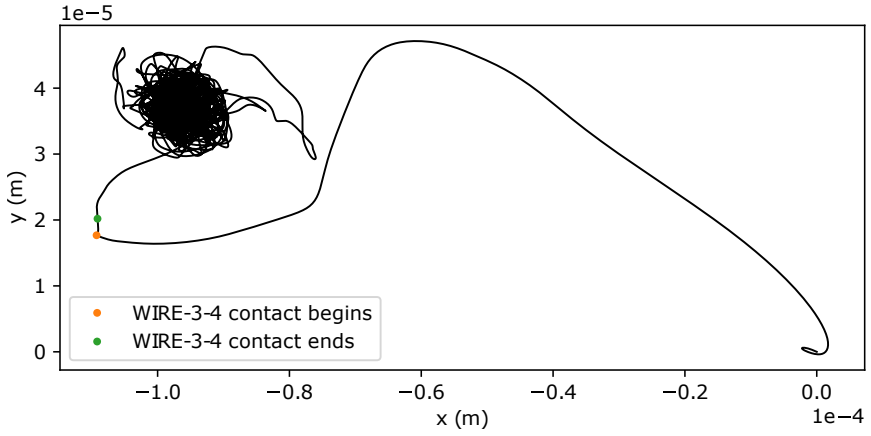

Figure 17: Trajectory of center pin centerline at $z = 0.7$ m for the case where $\mu = 0$. The time instants on which the contact situation changes is indicated with colored dots.

7.3. Displacement of the contact point

Displacement information is extracted at the contact positions too, allowing to evaluate the local behavior in more detail. It is also attempted to derive amplitude information from this, since this can be useful input for fretting experiments.

The trajectory of the contact locations of the central pin with $\mu = 0$ is depicted in Figure 18. Using Principle Component Analysis (PCA), the main directions in which the displacement occurs can be determined. The most important component is also displayed in Figure 18 and it is clear that for this case the trajectory fits well with a line. The same is done for the corner pin with $\mu = 0$ and also there it holds that the trajectory fits well with a line.

Projecting the 3D displacement on the line allows to come up with a first amplitude definition, namely the standard deviation of this signal. In addition, the velocity can be estimated by taking the time derivative. With this one-dimensional velocity information, direction switches can be detected as the velocity crossing zero. This allows three other amplitude definitions: the average displacement between two direction switches of the 1D signal, 2D signal (pro-

jected on the two most important components resulting from the PCA) or 3D signal (the original displacement data). The results are summarized in Table 7. The amplitudes found here are similar regardless of the definition, but they are an order of magnitude lower than those of the global vibration, reported in the previous section (see Figure 17).

Table 7: Amplitudes according to the different definitions for the central pin and corner pin with $\mu = 0$.

Pin	Amplitude definition	WIRE-6-1	ROD-6-3
Central pin ($\mu = 0$)	Standard deviation 1D	$1.7319 \times 10^{-6}\ m$	$2.0731 \times 10^{-6}\ m$
	Mean 1D distance	$1.7671 \times 10^{-6}\ m$	$2.2437 \times 10^{-6}\ m$
	Mean 2D distance	$1.7723 \times 10^{-6}\ m$	$2.2448 \times 10^{-6}\ m$
	Mean 3D distance	$1.7723 \times 10^{-6}\ m$	$2.2449 \times 10^{-6}\ m$
Pin	Amplitude definition	WIRE-HEX-6-1	WIRE-HEX-6-2
Corner pin ($\mu = 0$)	Standard deviation 1D	$1.7487 \times 10^{-6}\ m$	$1.7714 \times 10^{-6}\ m$
	Mean 1D distance	$2.3358 \times 10^{-6}\ m$	$1.9190 \times 10^{-6}\ m$
	Mean 2D distance	$2.3487 \times 10^{-6}\ m$	$1.9280 \times 10^{-6}\ m$
	Mean 3D distance	$2.3487 \times 10^{-6}\ m$	$1.9280 \times 10^{-6}\ m$

The given definitions are not generally applicable: when friction is implemented they sometimes break down due to sticking behavior. This can be clearly seen in Figure 19b. This trajectory is characterized by many sticking events and does not match well with the principle component for ROD-6-3, whereas it seems sound to apply the methodology to WIRE-6-1 (Figure 19a).

Since projecting the trajectory on a line does not work that well in this case, computing the standard deviation of this quantity is not believed a good estimate of the amplitude. Moreover, as the sticking events result in a multimodal displacement histogram, certain locations have a lot of weight in the computation of statistics because of a long-lasting sticking.

One could come up with an alternative definition, defining the amplitude as the average covered distance between two sticking events. However, for ROD-

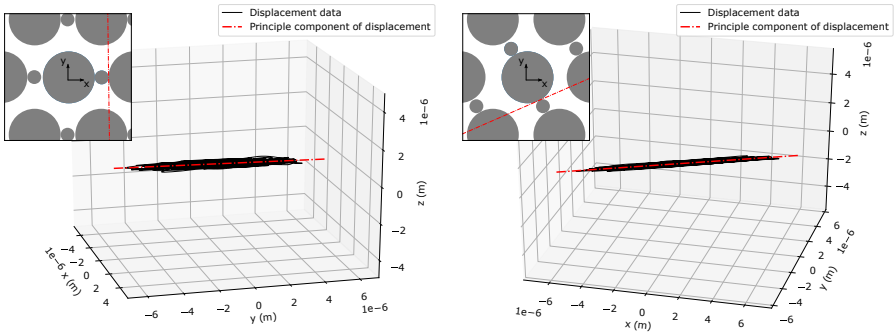

(a) (b)

Figure 18: Trajectory of contact point at location (a) WIRE-6-1 and (b) ROD-6-3 for the central pin with $\mu = 0$. The displacement is plotted, so the trajectory starts in the origin. The first component of a PCA is also shown with a red line. The inlay shows a cut of the bundle at the respective contact location, with the x- and y- component of the first component of the PCA again shown as a red line.

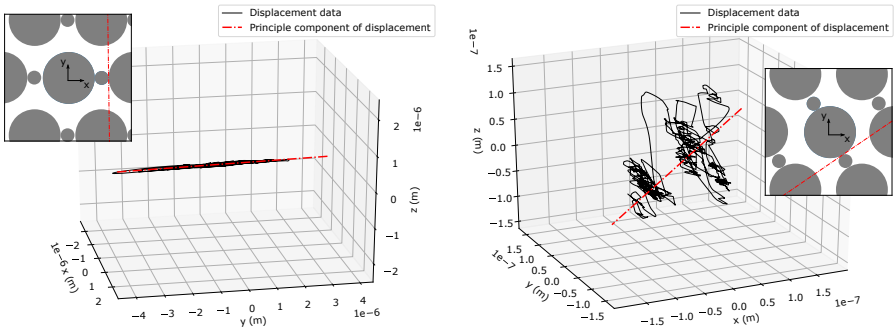

(a) (b)

Figure 19: Trajectory of contact point at location (a) WIRE-6-1 and (b) ROD-6-3 for the central pin with $\mu = 0.2$. The displacement is plotted, so the trajectory starts in the origin. The first component of a PCA is also shown with a red line. The inlay shows a cut of the bundle at the respective contact location, with the x- and y- component of the first component of the PCA again shown as a red line.

6-3 on the central pin with $\mu = 0.2$, the sticking takes up 86.69% of the time, which indicates that the amount of data gathered on sliding is too little to draw statistically meaningful conclusions, leaving the question unanswered if it is even relevant to characterize this specific case of contact by an amplitude definition. Because of the discussion above it is chosen to report only amplitudes for the frictionless cases (see Table 7), as they are more clear-cut.

7.4. Work rate

Before analyzing the time-averaged normal work rates, it is first verified whether the simulation time is long enough. In Figure 20 the work rate is plotted as a function of the length of the integration interval. The upper bound is held constant on the end of the simulation. In other words, the more right on the horizontal axis, the longer the integration interval. It can be seen that in the beginning it oscillates a lot. This is related to the instantaneous work rate terms of Eq. 13 forming a rather intermittent signal. As the forces are less intermittent in nature, their time averages converge much sooner. It is actually the velocity factor (Eq. 14) that renders the signal intermittent, especially when sticking occurs. It can be seen that when the integration interval is 2.5 seconds or longer, the result for the work rate (at WIRE-6-1) starts to stabilize, although some uncertainty remains. At the end, the graph can be seen to deviate again more from the stable result, especially for ROD-6-3. This is due to the transient (e.g. impacts) at the beginning of the simulation, since the end of the graph corresponds to including the entire simulation in the averaging. Because of this it is decided to omit the first 0.5 seconds.

From the discussion above it is concluded that sufficient simulation time for obtaining meaningful results starts from a duration of 3 seconds, allowing to omit the first 0.5 seconds and leaving at least 2.5 seconds for integration operations like computing the work rate and averaging of other quantities (see Table 6). The graph on Figure 20 shows the lesser convergence among all cases, so overall even a shorter integration time is deemed sufficient. All simulation lengths in Table 6 are therefore considered justified.

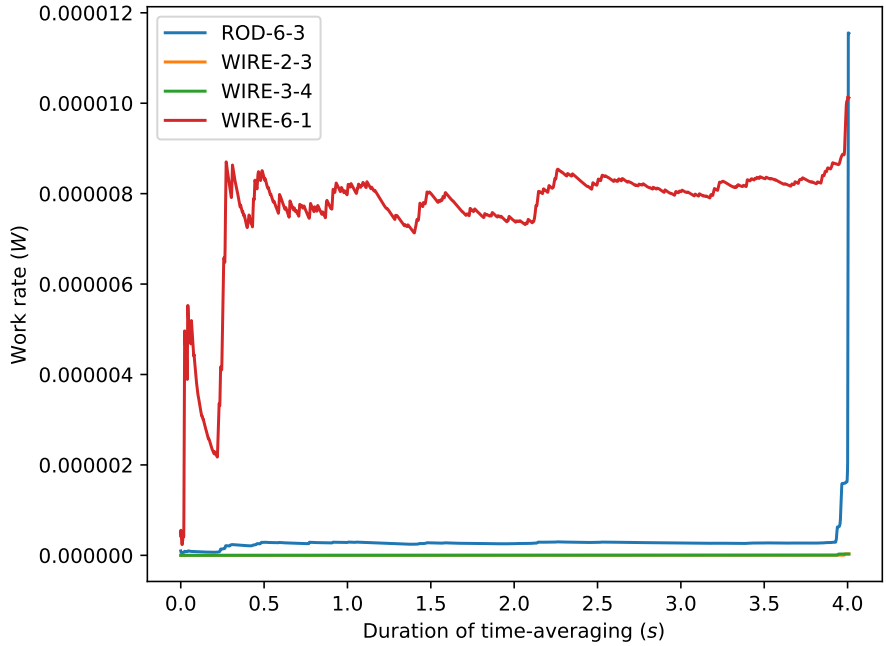

Figure 20: Time-averaged normal work rate convergence of the central pin as function of the duration of the time-averaging with constant end of integration window equal to the end of the simulation for the case where $\mu = 0.2$.

On Figure 21 and Figure 22 the instantaneous work rate terms of Eq. 13 are plotted versus the time, again for the central pin without friction and for the corner pin with $\mu = 0.1$. The signals indeed are highly intermittent, and large peaks are observed at the beginning of the simulation, as was the case for the normal forces.

For the central pin the location with the higher forces (ROD-6-3) also exhibits higher work rates. For the corner pin the difference is less clear, but the normal forces are also more evenly distributed between the contact locations in that case. The instantaneous work rates of the corner pin with $\mu = 0.1$ also are slightly more intermittent, remaining in the neighborhood of zero longer than in the frictionless case. This is the result of sticking behavior, as the frictionless cases never stick, while for the corner pin location WIRE-HEX-6-1 sticks 3% of

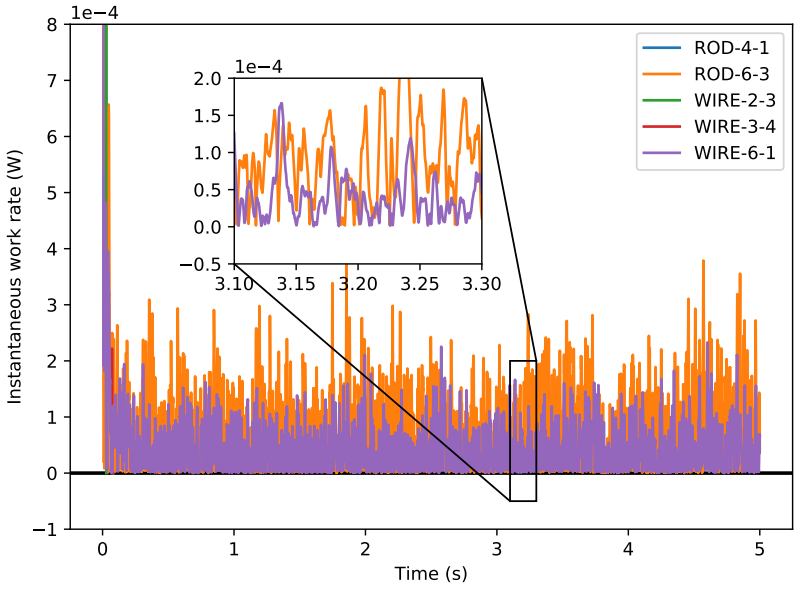

Figure 21: Instantaneous ork rates on the central pin for the case where $\mu = 0$.

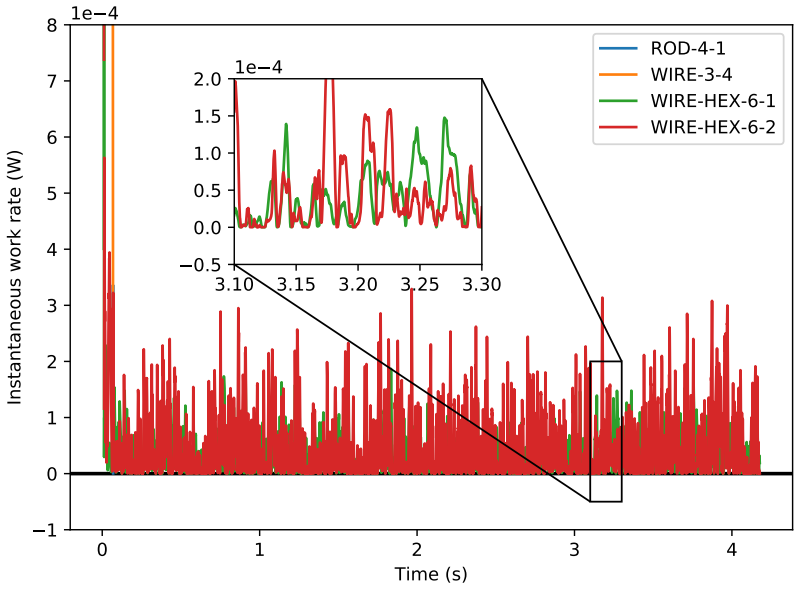

Figure 22: Instantaneous work rates on the corner pin for the case where $\mu = 0.1$.

the time and WIRE-HEX-6-2 sticks 9%. This effect becomes more pronounced when the friction factor is increased, as can be seen for example when looking at Figure 23 which depicts the instantaneous work rate for the central pin with $\mu = 0.2$.

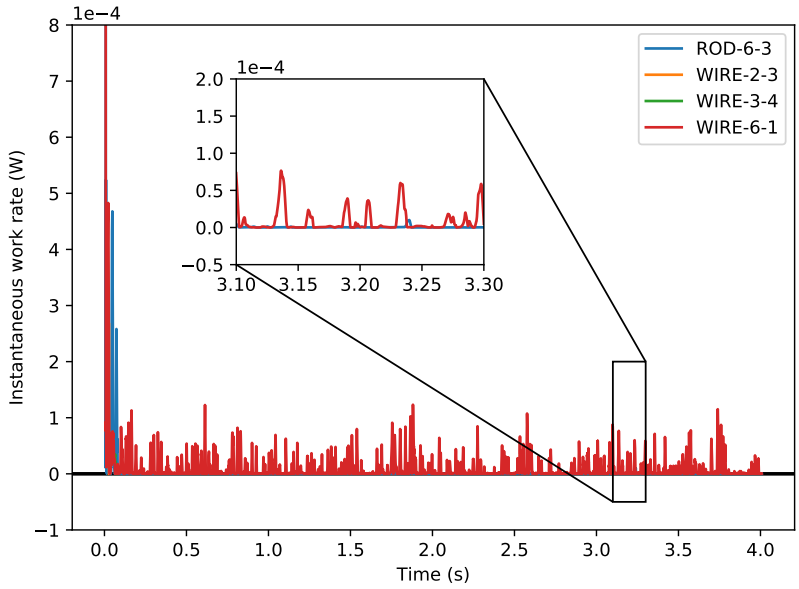

Figure 23: Instantaneous work rates on the central pin for the case where $\mu = 0.2$.

7.5. Effect of friction on the sticking behavior and work rate

In the following paragraphs relations between the friction coefficient μ, work rate $\dot{W}_N$ and sticking percentage are presented. The relations between the different quantities do not show a perfect correlation here, because other factors play a role as well in a complex fashion, such as the influence of the external excitation load and the geometry of the contact. Therefore the results are only qualitatively described.

Figure 24a shows the work rate of all contact locations plotted as function of μ (omitting the first 0.5 seconds from the time-averaging). For both the central and the corner pin, a descending trend is observed. This is in agreement

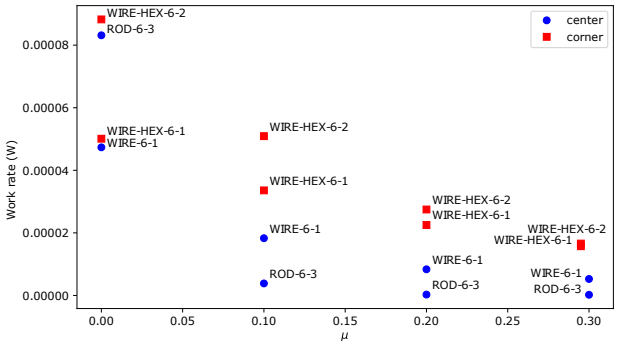

(a)

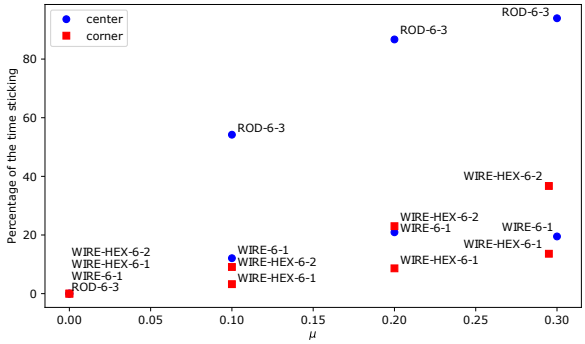

(b)

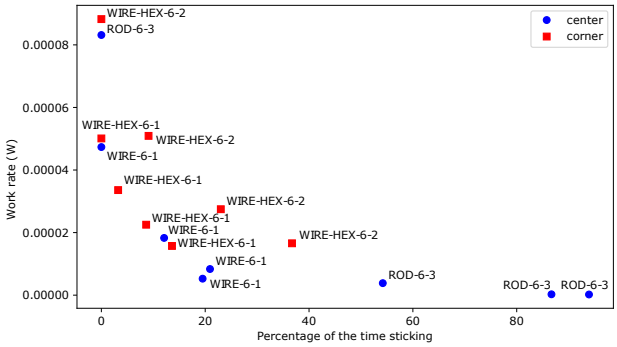

(c)

Figure 24: Summary of the results for all cases: (a) the time-averaged work rate at each contact location as function of μ, (b) the sticking percentage as function of μ and (c) the work rate at each contact location as function of the sticking percentage.

with observations in literature: since friction impedes sliding movement it has a direct negative impact on the work rate [43, 45, 50, 56, 72].

It can indeed be seen from Figure 24b that higher friction coefficients are associated with higher stick percentages. When plotting the work rate of each contact location against this stick ratio in Figure 24c, again a descending relationship can be discerned for each location. For the frictionless simulations, the observed work rates are rather similar between the central pin and corner pin. However no general conclusion can be drawn if this would always be the case, as only two pins have been investigated.

The highest observed work rate of about 8.82×10^{-5} W occurs for position WIRE-HEX-2, on the corner pin, when there is no friction simulated. A slightly lower work rate is observed for ROD-6-3 on the central pin, also without friction. Interesting here to note is that, while this position experiences the highest work rate for the frictionless case, it experiences the lowest work rate as soon as friction is modeled. This is attributed to the pronounced sticking that occurs for this location, which starts from 50% as can be seen from Figure 24b.

7.6. Estimation of the wear

The obtained results are finally employed to investigate the wear, which can be quantified as a volume removal rate as shown by Eq. 11. From experiments in the FRETHME facility at KIT [70, 73] it is known that the specific wear coefficient K for the cladding material ranges between 5×10^{-24} Pa^{-1} and 2×10^{-21} Pa^{-1} depending on the circumstances. Also a value of 2×10^{-17} Pa^{-1} was observed, but this is considered an outlier [73]. The test material was prepared by the Belgian Nuclear Research Centre and is representative for the MYRRHA fuel pins. 15-15Ti stabilized austenitic steel with a specific degree of cold working was used ($0.08 - 0.1$ wt% C, $14 - 16$ wt% Cr, $14 - 16$ wt% Ni, $0.3 - 0.5$ wt% Ti, $1.8 - 2.0$ wt% Mn and $1.3 - 1.7$ wt% Mo). One specimen was given the diameter of the rod and the other one the diameter of the wire. They were put at a perpendicular position, as a parallel configuration resulted in errors due to misalignment. The LBE was kept at a temperature of $400°$ C

and an oxygen concentration of 10^{-7} $wt\%$. A sliding frequency of 10 Hz was applied, with loads between 9 N and 75 N. The sliding amplitude was varied between 7.5 μm and 300 μm. Using 3D profilometry the wear volume and wear depth were determined. For more details the reader is referred to [73]. One can note that the experimental conditions are not exactly the same as in this work, but to the authors' knowledge these are the most representative available experimental values. As the sliding amplitudes and normal forces observed in this work are lower, it is difficult to select a representative K-value and compute a wear volume with it. To be conservative the highest measured value of K (neglecting the outlier) is considered: 2×10^{-21} Pa^{-1}, but still the results should be interpreted with care.

Instead of a volume removal rate, a penetration rate is more of interest to the operation of a reactor, as this quantity expresses how long it takes to wear through the cladding material. Since both the volume removal and wear depth have been measured, these quantities can be related to each other. The ratio between those two quantities can be considered as a measure of the wear scar area. For a Hertzian contact between perpendicular cylinders, it is known that this area is proportional to the normal force with an exponent of 2/3 [77],

$$V \propto h \cdot A \propto h \cdot F_N^{2/3}, \tag{15}$$

with h the penetration depth and A the area of the scar. This permits writing the wear depth resulting from the simulations h_{sim} as:

$$h_{sim} = \frac{V_{sim}}{V_{exp}} \cdot h_{exp} \cdot \left(\frac{F_{N,\ exp}}{F_{N,\ sim}} \right)^{2/3}, \tag{16}$$

where sim denotes quantity corresponding to simulation results and exp to measurements. For V_{exp} and h_{exp} the longest experiment (4080 hours) is selected, with a force of 10 N and amplitude of 60 μm. The ratio V_{exp}/h_{exp} lies just above the average ratio of all experiments, which were mostly short-term (100 - 500 hours). Using Archard's law (see Eq. 11) $\dot{V}_{sim}$ can be computed, resulting in the following expression for the wear rate $\dot{h}_{sim}$:

$$\dot{h}_{sim} = \frac{K \cdot \dot{W}_N}{V_{exp}} \cdot h_{exp} \cdot \left(\frac{F_{N,\ exp}}{F_{N,\ sim}} \right)^{2/3}. \tag{17}$$

This computation can be repeated for all contact locations and the result is plotted in Figure 25. The penetration rate can be seen to decrease with increasing friction coefficient, which indicates that the frictionless simulations yield a conservative estimate. The highest values are found on the locations where the highest work rates were observed (see Figure 24a) and vice versa.

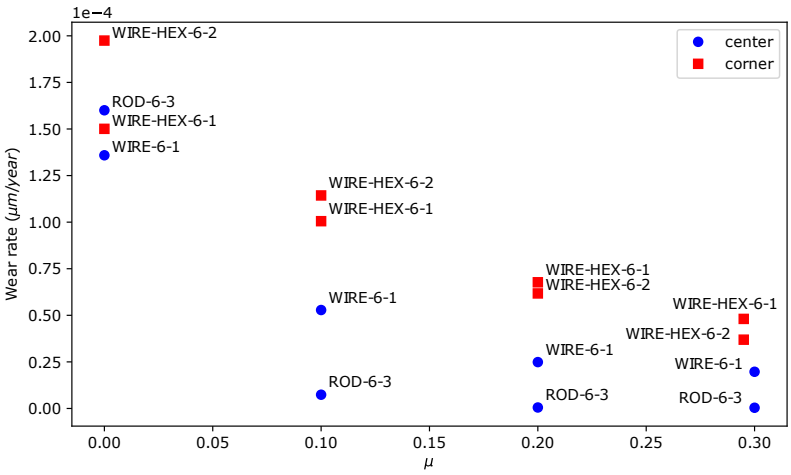

Figure 25: Wear rate $\dot{h}$ for each contact location against μ, predicted from simulation results combined with experimental results.

A maximal penetration depth h_{max} of 150 μm is aimed for, while a fuel pin should reside in the reactor for 3 years, yielding a maximal penetration rate of 50 $\mu m/year$. The obtained wear rates are much lower and are at most 2×10^{-4} $\mu m/year$, but one should be cautious drawing conclusions from this as the amplitude and normal force magnitude in the fretting tests were different, which introduces uncertainty in the value of K. Fretting experiments at lower amplitude and force could prove useful for a better estimation of the expected wear rate.

Recent experimental work of Nixon [78] succeeded to measure the displacement dynamics and detect the contact locations in a 19-pin bundle subject to water flow and with similar boundary conditions as current work. A corner pin

was investigated (as was the case here), but at a different location with respect to the mounting rails, so more comparable to pin 5B in Figure 7. Contacts were observed with the hexagonal duct and two adjacent pins equivalent to 4C and 5C. The pins of the inner ring (like 5A) were not measured. The contacts with the other pins were found to occur along the entire length. A direct comparison is however difficult due to the different working fluid and geometric properties, such as the pitch-to-diameter ratio and helical-pitch-to-diameter ratio. The pin is also shorter and the number of wire pitches is almost integer (about 4), which can have an effect on the static deformation [13]. In the current work it was observed that contact mostly occurs near the downstream end.

Contact at the end pieces is a beneficial situation, since no fuel is present there. It should however be noted, on the one hand, that in reality, the neighboring fuel pins are not rigid and bow could be present due to fuel deformations, which could likely result in contact at other locations as well. More research towards deformed bundles is needed to be able to predict if this deteriorates the fretting wear. On the other hand, cold conditions are investigated, with clearances between the rods. In reality, these gaps will close up due to thermal expansion of the fuel bundle, which could have a large influence on the wear. Besides that, also irradiation-induced swell and bow of the pins can contribute to the clearance reduction. This effect is not investigated here, but in literature [79] it is hypothesized that it could reduce vibration as there is less freedom of movement and moreover result in preloads at the contact location. Preloads influence the work rate, both directly (see Eq. 12) and through its effect on the sliding. Preload was observed to reduce wear in fretting tests for PWR [39]. Also in numerical work for PWR it was found that high preloads prevent wear by impeding sliding motion, while moderate preload maximized the wear [55].

8. Conclusion

Turbulence-induced vibrations of a 19-pin fuel assembly representative for the MYRRHA reactor were numerically investigated in a joint effort between

the Belgian Nuclear Research Center, Argonne National Laboratory and Ghent University.

Currently it is computationally expensive to simulate fluid-structure interactions of a large and complex domain using two-way coupling involving a LES model. Therefore, a multi-stage procedure was devised that covers the relevant physical aspects in dedicated models and combines them to achieve an efficient prediction of turbulence-induced vibration. Contact interactions were also implemented, resulting in contact forces, work rates and an overall estimation of the fretting wear in the conditions under investigation.

Contact occurred predominantly at more downstream locations, opposite to the side where the fuel pins are mounted. It remains to be investigated whether this would hold when going to more realistic situations, where all pins are allowed to deform, thermal expansion occurs and possible assembly bow develops.

The friction coefficient has a moderating influence on the work rates, which can be attributed to its effect on the sliding motion. This effect was most clearly visible in the stick ratio, which increased with increasing friction coefficient.

The wear rate was estimated, making some conservative assumptions on the nature of the contact and using experimental measurements. The obtained values were low, but not deemed impossible. Moreover they comply to the provided wear constraints for MYRRHA. This result should however be interpreted cautiously, as the simulated conditions may differ from real operation. Additionally, these conditions were different from the experimental ones, expressing the need to investigate the evolution of fretting wear under the amplitude and load predicted by the simulations.

The order of magnitude of the contact forces was found to be around $0.1 - 0.5\ N$, while for the amplitude of the sliding motion about $2 \times 10^{-6}\ m$ was found. These results can facilitate future experiments to investigate fretting wear. While no definite conclusion about the fretting wear in MYRRHA can be drawn, the proposed methodology proves useful to build future work upon and provides insight in the behavior of the assembly under fluid loads.

Acknowledgements

This work was performed in the framework of the Horizon 2020 MYRTE Project. It has received funding from the Euratom research and training program 2014–2018 under grant agreement No. 662186 (MYRTE).

The computational resources (Stevin Supercomputer Infrastructure) and services used in this work were provided by the VSC (Flemish Supercomputer Center), funded by Ghent University, FWO and the Flemish Government – department EWI.

Thanks to Prof. Dieter Fauconnier for sharing his insight in the tribology aspects.

The authors wish to express their gratitude to professor Jan Vierendeels, who passed away in 2018, for his contribution to the early phases of this work and the research field in general.

References

[1] J. Engelen, H. Aït Abderrahim, P. Baeten, D. De Bruyn, P. Leysen, MYRRHA: Preliminary front-end engineering design, International Journal of Hydrogen Energy 40 (44) (2015) 15137–15147. doi:https://doi.org/10.1016/j.ijhydene.2015.03.096.

[2] M. P. Païdoussis, A review of flow-induced vibrations in reactors and reactor components, Nuclear Engineering and Design 74 (1) (1983) 31–60. doi:https://doi.org/10.1016/0029-5493(83)90138-3.

[3] R. Gajapathy, K. Velusamy, P. Selvaraj, P. Chellapandi, CFD investigation of effect of helical wire-wrap parameters on the thermal hydraulic performance of 217 fuel pin bundle, Annals of Nuclear Energy 77 (2015) 498–513. doi:https://doi.org/10.1016/j.anucene.2014.10.038.

[4] J.-H. Jeong, M.-S. Song, K.-L. Lee, Thermal-hydraulic effect of wire spacer in a wire-wrapped fuel bundles for SFR, Nuclear Engineering and Design

320 (2017) 28–43. doi:https://doi.org/10.1016/j.nucengdes.2017.05.019.

[5] J.-H. Jeong, J. Yoo, K.-L. Lee, K.-S. Ha, Three-dimensional flow phenomena in a wire-wrapped 37-pin fuel bundle for SFR, Nuclear Engineering and Technology 47 (5) (2015) 523–533. doi:https://doi.org/10.1016/j.net.2015.06.001.

[6] I. Ahmad, K.-Y. Kim, Three-dimensional analysis of flow and heat transfer in a wire-wrapped fuel assembly, in: International Congress on Advances in Nuclear Power Plants 2005, ICAPP'05, Vol. 1, American Nuclear Society (ANS).

[7] W. Raza, K.-Y. Kim, Effects of wire-spacer shape in LMR on thermal–hydraulic performance, Nuclear Engineering and Design 238 (10) (2008) 2678–2683. doi:https://doi.org/10.1016/j.nucengdes.2008.05.003.

[8] K. D. Hamman, R. A. Berry, A CFD simulation process for fast reactor fuel assemblies, Nuclear Engineering and Design 240 (9) (2010) 2304–2312. doi:https://doi.org/10.1016/j.nucengdes.2009.11.007.

[9] T. Sreenivasulu, B. V. S. S. S. Prasad, Flow and heat transfer characteristics in a seven tube-bundle wrapped with helical wires, International Journal of Advancements in Technology 2 (3) (2011) 350–381.

[10] S. Rolfo, C. Péniguel, M. Guillaud, D. Laurence, Thermal-hydraulic study of a wire spacer fuel assembly, Nuclear Engineering and Design 243 (2012) 251–262. doi:https://doi.org/10.1016/j.nucengdes.2011.11.021.

[11] E. Merzari, P. Fischer, H. Yuan, K. Van Tichelen, S. Keijers, J. De Ridder, J. Degroote, J. Vierendeels, H. Doolaard, V. R. Gopala, F. Roelofs, Benchmark exercise for fluid flow simulations in a liquid metal fast reactor fuel assembly, Nuclear Engineering and Design 298 (2016) 218–228. doi:https://doi.org/10.1016/j.nucengdes.2015.11.002.

[12] L. Brockmeyer, L. B. Carasik, E. Merzari, Y. Hassan, Numerical simulations for determination of minimum representative bundle size in wire wrapped tube bundles, Nuclear Engineering and Design 322 (2017) 577–590. doi:https://doi.org/10.1016/j.nucengdes.2017.06.038.

[13] D. De Santis, A. Shams, Analysis of flow induced vibrations and static deformations of fuel rods considering the effects of wire spacers and working fluids, Journal of Fluids and Structures 84 (2019) 440–465. doi:https://doi.org/10.1016/j.jfluidstructs.2018.11.015.

[14] M. Martin, D. Leonard, R. B. Jackson, K. M. Steer, CFD verification and validation of wire-wrapped pin assemblies, Nuclear Technology 206 (9) (2020) 1325–1336. doi:10.1080/00295450.2020.1727263.

[15] P. Fischer, J. Lottes, A. Siegel, G. Palmiotti, Large eddy simulation of wire-wrapped fuel pins I: Hydrodynamics in a periodic array, Report (2007).

[16] E. Merzari, W. D. Pointer, J. G. Smith, A. Tentner, P. Fischer, Numerical simulation of the flow in wire-wrapped pin bundles: Effect of pin-wire contact modeling, Nuclear Engineering and Design 253 (2012) 374–386. doi:https://doi.org/10.1016/j.nucengdes.2011.09.030.

[17] L. Brockmeyer, A. Obabko, E. Merzari, Y. Hassan, Analysis of pressure field on wire-wrapped pin bundle surface for concerns of FSI, in: ASME 2018 5th Joint US-European Fluids Engineering Division Summer Meeting, 2018. doi:10.1115/fedsm2018-83521.

[18] L. Brockmeyer, E. Merzari, J. Solberg, Y. Hassan, One-way coupled simulation of FIV in a 7-pin wire-wrapped fuel pin bundle, Nuclear Engineering and Design 356 (2020) 110367. doi:https://doi.org/10.1016/j.nucengdes.2019.110367.

[19] S. Kottapalli, A. Shams, A. H. Zuijlen, M. J. B. M. Pourquie, Numerical investigation of an advanced U-RANS based pressure fluctuation model to

simulate non-linear vibrations of nuclear fuel rods due to turbulent parallel-flow, Annals of Nuclear Energy 128 (2019) 115–126. doi:https://doi.org/10.1016/j.anucene.2019.01.001.

[20] D. De Santis, A. Shams, An advanced numerical framework for the simulation of flow induced vibration for nuclear applications, Annals of Nuclear Energy 130 (2019) 218–231. doi:https://doi.org/10.1016/j.anucene.2019.02.049.

[21] F. Roelofs, Thermal hydraulics aspects of liquid metal cooled nuclear reactors, Woodhead Publishing, 2019.

[22] S. Benhamadouche, P. Moussou, C. Le Maitre, CFD estimation of the flow-induced vibrations of a fuel rod downstream a mixing grid, in: ASME 2009 Pressure Vessels and Piping Conference, Vol. Volume 4: Fluid-Structure Interaction, 2009, pp. 489–497. doi:10.1115/pvp2009-78054.

[23] A. Elmahdi, R. Lu, M. Conner, Z. Karoutas, E. Baglietto, Flow induced vibration forces on a fuel rod by LES CFD analysis, in: The 14th International Topical Meeting on Nuclear Reactor Thermal Hydraulics (NURETH-14), 2011.

[24] M. A. Christon, R. Lu, J. Bakosi, B. T. Nadiga, Z. Karoutas, M. Berndt, Large-eddy simulation, fuel rod vibration and grid-to-rod fretting in pressurized water reactors, Journal of Computational Physics 322 (2016) 142–161. doi:https://doi.org/10.1016/j.jcp.2016.06.042.

[25] Z. G. Liu, Y. Liu, J. Lu, Fluid–structure interaction of single flexible cylinder in axial flow, Computers & Fluids 56 (2012) 143–151. doi:https://doi.org/10.1016/j.compfluid.2011.12.003.

[26] Z. G. Liu, Y. Liu, J. Lu, Numerical simulation of the fluid–structure interaction for an elastic cylinder subjected to tubular fluid flow, Computers & Fluids 68 (2012) 192–202. doi:https://doi.org/10.1016/j.compfluid.2012.08.010.

[27] Z. G. Liu, Y. Liu, J. Lu, Numerical simulation of the fluid–structure interaction for two simple fuel assemblies, Nuclear Engineering and Design 258 (2013) 1–12. doi:https://doi.org/10.1016/j.nucengdes.2013.01.029.

[28] J. Degroote, Partitioned simulation of fluid-structure interaction, Archives of Computational Methods in Engineering 20 (3) (2013) 185–238. doi:10.1007/s11831-013-9085-5.

[29] T. Nazari, A. Rabiee, H. Kazeminejad, Two-way fluid-structure interaction simulation for steady-state vibration of a slender rod using URANS and LES turbulence models, Nuclear Engineering and Technology 51 (2) (2019) 573–578. doi:https://doi.org/10.1016/j.net.2018.10.011.

[30] J. D. Hooper, K. Rehme, Large-scale structural effects in developed turbulent flow through closely-spaced rod arrays, Journal of Fluid Mechanics 145 (1984) 305–337. doi:10.1017/S0022112084002949.

[31] J. De Ridder, J. Degroote, K. Van Tichelen, P. Schuurmans, J. Vierendeels, Modal characteristics of a flexible cylinder in turbulent axial flow from numerical simulations, Journal of Fluids and Structures 43 (2013) 110–123. doi:https://doi.org/10.1016/j.jfluidstructs.2013.09.001.

[32] D. De Santis, A. Shams, Numerical modeling of flow induced vibration of nuclear fuel rods, Nuclear Engineering and Design 320 (2017) 44–56. doi:https://doi.org/10.1016/j.nucengdes.2017.05.013.

[33] D. De Santis, S. Kottapalli, A. Shams, Numerical simulations of rod assembly vibration induced by turbulent axial flows, Nuclear Engineering and Design 335 (2018) 94–105. doi:https://doi.org/10.1016/j.nucengdes.2018.04.027.

[34] S.-S. Chen, Vibration of nuclear fuel bundles, Nuclear Engineering and Design 35 (3) (1975) 399–422. doi:https://doi.org/10.1016/0029-5493(75)90071-0.

[35] S. S. Chen, Dynamics of heat exchanger tube banks, Journal of Fluids Engineering 99 (3) (1977) 462–467. doi:10.1115/1.3448815.

[36] J. De Ridder, J. Degroote, K. Van Tichelen, J. Vierendeels, Predicting modal characteristics of a cluster of cylinders in axial flow: From potential flow solutions to coupled CFD–CSM calculations, Journal of Fluids and Structures 74 (2017) 90–110. doi:https://doi.org/10.1016/j.jfluidstructs.2017.07.006.

[37] J. De Ridder, J. Degroote, K. V. Tichelen, P. Schuurmans, J. Vierendeels, Predicting turbulence-induced vibration in axial annular flow by means of large-eddy simulations, Journal of Fluids and Structures 61 (2016) 115–131. doi:https://doi.org/10.1016/j.jfluidstructs.2015.10.011.

[38] R. G. Sauvé, M. Tabatabai, G. Morandin, M. Kozluk, Application of flow-induced vibration predictive techniques to operating steam generators, in: Proceedings of the Third International Conference on Heat Exchangers and Steam Generators, 1998.

[39] K.-T. Kim, The study on grid-to-rod fretting wear models for PWR fuel, Nuclear Engineering and Design 239 (12) (2009) 2820–2824. doi:https://doi.org/10.1016/j.nucengdes.2009.08.018.

[40] Z.-b. Cai, Z.-y. Li, M.-g. Yin, M.-h. Zhu, Z.-r. Zhou, A review of fretting study on nuclear power equipment, Tribology International 144 (2020) 106095. doi:https://doi.org/10.1016/j.triboint.2019.106095.

[41] R. J. Rogers, R. J. Pick, On the dynamic spatial response of a heat exchanger tube with intermittent baffle contacts, Nuclear Engineering and Design 36 (1) (1976) 81–90. doi:https://doi.org/10.1016/0029-5493(76)90144-8.

[42] R. J. Rogers, R. J. Pick, Factors associated with support plate forces due to heat-exchanger tube vibratory contact, Nuclear Engineering and Design

44 (2) (1977) 247–253. doi:https://doi.org/10.1016/0029-5493(77)90031-0.

[43] J. Antunes, F. Axisa, B. Beaufils, D. Guilbaud, Coulomb friction modelling in numerical simulations of vibration and wear work rate of multispan tube bundles, Journal of Fluids and Structures 4 (3) (1990) 287–304. doi:https://doi.org/10.1016/S0889-9746(05)80016-7.

[44] M. A. Hassan, D. S. Weaver, M. A. Dokainish, A simulation of the turbulence response of heat exchanger tubes in lattice-bar supports, Journal of Fluids and Structures 16 (8) (2002) 1145–1176. doi:https://doi.org/10.1006/jfls.2002.0468.

[45] M. A. Hassan, D. S. Weaver, M. A. Dokainish, The effects of support geometry on the turbulence response of loosely supported heat exchanger tubes, Journal of Fluids and Structures 18 (5) (2003) 529–554. doi:https://doi.org/10.1016/j.jfluidstructs.2003.08.011.

[46] G. D. Morandin, R. G. Sauvé, Probabilistic assessment of fretting wear in steam generator tubes under flow induced vibrations, in: ASME 2003 Pressure Vessels and Piping Conference, 2003, pp. 117–125. doi:10.1115/pvp2003-2081.

[47] M. Hassan, A. Mohany, A numerical characterization of flow-induced vibration and fretting wear potential in nuclear steam generator tube bundles, in: ASME 2011 Pressure Vessels and Piping Conference, Vol. Volume 4: Fluid-Structure Interaction, 2011, pp. 141–149. doi:10.1115/pvp2011-57182.

[48] M. Hassan, J. Riznic, Evaluation of the integrity of steam generator tubes subjected to flow induced vibrations, Journal of Pressure Vessel Technology 136 (5). doi:10.1115/1.4026982.

[49] M. Hassan, A. Mohany, Simulations of fluidelastic forces and fretting wear in U-bend tube bundles of steam generators: Effect of tube-support conditions, Wind and Structures 23. doi:10.12989/WAS.2016.23.2.157.

[50] M. Yetisir, N. J. Fisher, Prediction of pressure tube fretting-wear damage due to fuel vibration, Nuclear Engineering and Design 176 (3) (1997) 261–271. doi:https://doi.org/10.1016/S0029-5493(97)00149-0.

[51] A. Mohany, M. Hassan, Modelling of fuel bundle vibration and the associated fretting wear in a candu fuel channel, Nuclear Engineering and Design 264 (2013) 214–222. doi:https://doi.org/10.1016/j.nucengdes.2012.08.039.

[52] O. Elbanhawy, M. Hassan, A. Mohany, Simulations of fully-flexible fuel bundle response due to turbulence excitation, in: ASME 2019 Pressure Vessels & Piping Conference, Vol. Volume 4: Fluid-Structure Interaction, 2019. doi:10.1115/pvp2019-93790.

[53] M. Fadaee, S. D. Yu, A comprehensive dynamic model for analysing the vibrational behaviour of a candu fuel string, Progress in Nuclear Energy 107 (2018) 193–204. doi:https://doi.org/10.1016/j.pnucene.2018.04.007.

[54] K.-T. Kim, The effect of fuel rod supporting conditions on fuel rod vibration characteristics and grid-to-rod fretting wear, Nuclear Engineering and Design 240 (6) (2010) 1386–1391. doi:https://doi.org/10.1016/j.nucengdes.2009.12.030.

[55] P. R. Rubiolo, Probabilistic prediction of fretting-wear damage of nuclear fuel rods, Nuclear Engineering and Design 236 (14) (2006) 1628–1640. doi:https://doi.org/10.1016/j.nucengdes.2006.04.023.

[56] P. R. Rubiolo, M. Y. Young, On the factors affecting the fretting-wear risk of PWR fuel assemblies, Nuclear Engineering and Design 239 (1) (2009) 68–79. doi:https://doi.org/10.1016/j.nucengdes.2008.08.021.

[57] K. Van Tichelen, G. Kennedy, F. Mirelli, A. Marino, A. Toti, D. Rozzia, E. Cascioli, S. Keijers, P. Planquart, Advanced liquid-metal thermal-

hydraulic research for MYRRHA, Nuclear Technology 206 (2) (2020) 150–163. doi:10.1080/00295450.2019.1614803.

[58] G. Kennedy, K. Van Tichelen, J. Pacio, I. Di Piazza, H. Uitslag-Doolaard, Thermal-hydraulic experimental testing of the MYRRHA wire-wrapped fuel assembly, Nuclear Technology 206 (2) (2020) 179–190. doi:10.1080/00295450.2019.1620539.

[59] A. Otsubo, T. Okada, N. Takahashi, K. Sato, N. Hattori, The occurrence of wear marks on fast reactor fuel pin cladding, Journal of Nuclear Science and Technology 36 (6) (1999) 522–534. doi:10.1080/18811248.1999.9726234.

[60] B. De Pauw, Experimental analysis of flow-induced vibration in lead-bismuth cooled nuclear fuel assemblies, Ph.D. thesis (2015).

[61] B. De Pauw, S. Vanlanduit, K. Van Tichelen, T. Geernaert, K. Chah, F. Berghmans, Benchmarking of deformation and vibration measurement techniques for nuclear fuel pins, Measurement 46 (9) (2013) 3647–3653. doi:https://doi.org/10.1016/j.measurement.2013.07.003.

[62] J. Degroote, K.-J. Bathe, J. Vierendeels, Performance of a new partitioned procedure versus a monolithic procedure in fluid–structure interaction, Computers & Structures 87 (11) (2009) 793–801. doi:https://doi.org/10.1016/j.compstruc.2008.11.013.

[63] E. Merzari, P. Fischer, M. Min, S. Kerkemeier, A. Obabko, D. Shaver, H. Yuan, Y. Yu, J. Martinez, L. Brockmeyer, L. Fick, G. Busco, A. Yildiz, Y. Hassan, Toward exascale: Overview of large eddy simulations and direct numerical simulations of nuclear reactor flows with the spectral element method in Nek5000, Nuclear Technology (2020) 1–17doi:10.1080/00295450.2020.1748557.

[64] V. Sobolev, G. Benamati, Thermophysical and electric properties, Vol. 1, OECD NEA - Nuclear Energy Agency, Paris, France, 2007, pp. 25–99.

[65] M. A. Hassan, D. S. Weaver, M. A. Dokainish, A new tube/support impact model for heat exchanger tubes, Journal of Fluids and Structures 21 (5) (2005) 561–577. doi:https://doi.org/10.1016/j.jfluidstructs.2005.07.016.

[66] M. A. Hassan, R. J. Rogers, Friction modelling of preloaded tube contact dynamics, Nuclear Engineering and Design 235 (22) (2005) 2349–2357. doi:https://doi.org/10.1016/j.nucengdes.2005.05.004.

[67] Y. Saad, Numerical methods for large eigenvalue problems: revised edition, SIAM, 2011.

[68] D. De Santis, A. Shams, Scaling of added mass and added damping of cylindrical rods by means of FSI simulations, Journal of Fluids and Structures 88 (2019) 241–256. doi:https://doi.org/10.1016/j.jfluidstructs.2019.05.011.

[69] C. E. Taylor, M. J. Pettigrew, T. J. Dickinson, I. G. Currie, P. Vidalou, Vibration damping in multispan heat exchanger tubes, Journal of Pressure Vessel Technology 120 (3) (1998) 283–289. doi:10.1115/1.2842059.

[70] M. Del Giacco, Investigation of fretting wear of cladding materials in liquid lead, Ph.D. thesis (2013). doi:10.5445/ksp/1000031949.

[71] P. L. Ko, Wear of power plant components due to impact and sliding, Applied Mechanics Reviews 50 (7) (1997) 387–411. doi:10.1115/1.3101724.

[72] C. Phalippou, X. Delaune, The predictive analysis of wear work-rates in wear test rigs, American Society of Mechanical Engineers, Pressure Vessels and Piping Division (Publication) PVP 328 (1996) 247–256.

[73] A. Heinzel, A. Weisenburger, Report on the fretting test with MYRRHA relevant design and conditions. MYRTE Deliverable 3.23, Report (2019).

[74] M. H. Choi, H. S. Kang, K. H. Yoon, K. N. Song, Vibration analysis of a dummy fuel rod continuously supported by spacer grids, Nuclear Engineer-

ing and Design 232 (2) (2004) 185–196. doi:https://doi.org/10.1016/j.nucengdes.2003.11.007.

[75] H. J. Connors, Flow-induced vibration and wear of steam generator tubes, Nuclear Technology 55 (2) (1981) 311–331. doi:10.13182/NT55-311.

[76] B. Fontaine, I. Politopoulos, A non linear model for the PWR fuel assembly seismic analysis, Nuclear Engineering and Design 195 (3) (2000) 321–329. doi:https://doi.org/10.1016/S0029-5493(99)00217-4.

[77] V. Popov, Contact Mechanics and Friction: Physical Principles and Applications, 1st Edition, Springer-Verlag Berlin Heidelberg, 2010. doi:10.1007/978-3-642-10803-7.

[78] C. A. Nixon, W. R. Marcum, K. M. Steer, R. B. Jackson, M. G. Martin, A. W. Weiss, On the fluid structure interactions of a wire-wrapped pin bundle, Nuclear Technology 206 (2) (2020) 218–230. doi:10.1080/00295450.2019.1649583.

[79] B. De Pauw, G. Kennedy, K. Van Tichelen, T. Geernaert, H. Thienpont, F. Berghmans, Characterizing flow-induced vibrations of fuel assemblies for future liquid metal cooled nuclear reactors using quasi-distributed fibre-optic sensors, Applied Sciences 7 (2017) 864. doi:10.3390/app7080864.